

01 Oct 2016

A Dual-Porosity-Stokes Model and Finite Element Method for Coupling Dual-Porosity Flow and Free Flow

Jiangyong Hou

Meilan Qiu


Xiaoming He

Missouri University of Science and Technology, hex@mst.edu

Chaohua Guo

et. al. For a complete list of authors, see https://scholarsmine.mst.edu/math_stat_facwork/696

Follow this and additional works at: https://scholarsmine.mst.edu/math_stat_facwork

 Part of the [Geology Commons](#), [Mathematics Commons](#), [Numerical Analysis and Scientific Computing Commons](#), and the [Statistics and Probability Commons](#)

Recommended Citation

J. Hou et al., "A Dual-Porosity-Stokes Model and Finite Element Method for Coupling Dual-Porosity Flow and Free Flow," *SIAM Journal on Scientific Computing*, vol. 38, no. 5, pp. B710-B739, Society for Industrial and Applied Mathematics (SIAM), Oct 2016.

The definitive version is available at <https://doi.org/10.1137/15M1044072>

This Article - Journal is brought to you for free and open access by Scholars' Mine. It has been accepted for inclusion in Mathematics and Statistics Faculty Research & Creative Works by an authorized administrator of Scholars' Mine. This work is protected by U. S. Copyright Law. Unauthorized use including reproduction for redistribution requires the permission of the copyright holder. For more information, please contact scholarsmine@mst.edu.

A DUAL-POROSITY-STOKES MODEL AND FINITE ELEMENT METHOD FOR COUPLING DUAL-POROSITY FLOW AND FREE FLOW*

JIANGYONG HOU[†], MEILAN QIU[‡], XIAOMING HE[§], CHAOHUA GUO[¶],
MINGZHEN WEI^{||}, AND BAOJUN BAI^{||}

Abstract. In this paper, we propose and numerically solve a new model considering confined flow in dual-porosity media coupled with free flow in embedded macrofractures and conduits. Such situation arises, for example, for fluid flows in hydraulic fractured tight/shale oil/gas reservoirs. The flow in dual-porosity media, which consists of both matrix and microfractures, is described by a dual-porosity model. And the flow in the macrofractures and conduits is governed by the Stokes equation. Then the two models are coupled through four physically valid interface conditions on the interface between dual-porosity media and macrofractures/conduits, which play a key role in a physically faithful simulation with high accuracy. All the four interface conditions are constructed based on fundamental properties of the traditional dual-porosity model and the well-known Stokes–Darcy model. The weak formulation is derived for the proposed model, and the well-posedness of the model is analyzed. A finite element semidiscretization in space is presented based on the weak formulation, and four different schemes are then utilized for the full discretization. The convergence of the full discretization with the backward Euler scheme is analyzed. Four numerical experiments are presented to validate the proposed model and demonstrate the features of both the model and the numerical method, such as the optimal convergence rate of the numerical solution, the detail flow characteristics around macrofractures and conduits, and the applicability to the real world problems.

Key words. dual-porosity model, Stokes equation, interface condition, multistage fractured horizontal wellbore

AMS subject classifications. 65M60, 65M12, 65M15, 35M10, 35Q35, 76D07, 76S05

DOI. 10.1137/15M1044072

1. Introduction. The coupling of porous media flow and free flow arises in many important applications, such as groundwater systems [27, 35, 36, 56, 62], industrial filtrations [40, 52, 70], petroleum extraction [3, 5, 6, 28, 90], biochemical transport [18, 33, 42, 73, 80], and so on. For this kind of coupled flow, the Stokes–Darcy model has been widely used and extensively investigated by many researchers during the past decade; see, e.g., [7, 8, 14, 17, 19, 21, 30, 37, 39, 43, 45, 49, 50, 59, 63, 65, 67, 68, 69, 74, 75, 84, 86, 87] and the references cited therein. The Stokes–Darcy model describes a coupled flow in a so-called porous media–conduit system in which a free

*Submitted to the journal’s Computational Methods in Science and Engineering section October 15, 2015; accepted for publication (in revised form) June 24, 2016; published electronically September 1, 2016.

<http://www.siam.org/journals/sisc/38-5/M104407.html>

Funding: The research of the third and fifth authors was partially supported by NSF grant DMS-1418624.

[†]Department of Mathematics, Northwest University, Xi’an, Shaanxi 710069, People’s Republic of China (mokufo@163.com).

[‡]Department of Mathematics, Huizhou University, Huizhou, Guangdong 516007, People’s Republic of China (meilanqiu16@163.com).

[§]Corresponding author. Department of Mathematics and Statistics, Missouri University of Science and Technology, Rolla, MO 65409 (hex@mst.edu).

[¶]Department of Petroleum Engineering, Missouri University of Science and Technology, Rolla, MO 65409. Current address: Department of Petroleum Engineering, China University of Geoscience, Wuhan, Hubei 430074, People’s Republic of China (cgqk7@mst.edu).

^{||}Department of Petroleum Engineering, Missouri University of Science and Technology, Rolla, MO 65409 (weim@mst.edu, baib@mst.edu).

flow and a porous medium flow occur in separate but abutting domains with the two flows coupled on the interface between the two domains.

The Darcy model in the traditional Stokes–Darcy system is a single porosity model, which is not accurate to describe the complicated porous media with multiple porosities. For example, a naturally fractured reservoir is comprised of low permeable rock matrix blocks surrounded by an irregular network of natural microfractures, and the matrix and microfractures have different fluid storage and conductivity properties [2, 82, 88]. The traditional dual-porosity models have been widely used to describe the naturally fractured porous media for different problems in hydrology, carbon sequestration, geothermal system, and petroleum extraction [4, 25, 32, 46, 47, 51, 53, 54, 61, 79, 91]. But this model itself does not consider the free flow in large conduits. On the other hand, none of the existing Stokes–Darcy models consider a dual-porosity model when they couple the porous media flow with the free flow. Therefore, based on the key idea of the traditional Stokes–Darcy model, in this paper we propose a new dual-porosity-Stokes model to govern the flow in the coupled system which consists of dual-porosity media and macrofractures/conduits.

A dual-porosity medium includes the matrix system and the microfracture system, which are generally assumed to involve two overlapping but interacting domains with different hydraulic and transport properties. The microfracture system is more permeable than the matrix system, while the matrix system has larger storage capacity compared with the microfracture system [2, 82]. The single phase dual-porosity model includes two equations, the matrix pressure equation and the microfracture pressure equation, which characterize the flow in the matrix medium and microfracture medium, respectively. These two equations are coupled through a mass exchange term which describes the fluids flowing from the matrix to the microfractures. Furthermore, in the traditional dual-porosity model, the description of the production from the microfracture medium to the wellbore is simplified as a source term in the microfracture equation.

In this paper, we propose, numerically solve, and analyze a new dual-porosity-Stokes model, which utilizes interface conditions to couple a dual-porosity model with the Stokes equation, for confined flow in dual-porosity media coupled with free flow in embedded conduits or macrofractures. The dual-porosity media include the matrix and the microfractures, and the conduits include the macrofractures and the wellbore, etc. The dual-porosity media and the conduits are two nonoverlapping but contiguous regions with interfaces between them. The dual-porosity model and the Stokes equation are used to govern the flow in dual-porosity media and conduits, respectively.

In contrast to the traditional Stokes–Darcy model, the new model uses two pressures, the matrix pressure and the fracture pressure, instead of only one pressure, to couple with the Stokes equations. Thus, four physically valid interface conditions are utilized to couple the two models on the interface between the dual-porosity media and the conduits, including a no-exchange condition, a mass balance condition, a force balance condition, and the Beavers–Joseph condition [10]. The first interface condition is proposed for the flow in the matrix based on a fundamental property of a dual-porosity model that the flow in matrix only goes into the microfractures but does not interact with conduits on the interface. Motivated by another fundamental property of a dual-porosity model that the flow exchange on the interface only happens between the microfractures and the conduits, the other three interface conditions are borrowed from the traditional Stokes–Darcy model to describe the flux transfer and exchange on the interface between the microfractures and the conduits.

To our best knowledge, this is the first work to model and simulate the coupled flow in a dual-porosity-conduit interface system. Therefore, after the weak formulation is first formed, a finite element method is proposed with four different time discretization schemes. We analyze the well-posedness of the model and the convergence of the full discretization with the backward Euler scheme. Four numerical experiments are also presented to show the features of the model and the finite element method. The first experiment shows that the optimal convergence order is obtained for the finite element method. The second experiment investigates the characteristics of the flow around natural macrofractures. In the third and fourth experiments, a horizontal wellbore with open-hole completion and a multistage fractured horizontal wellbore (MsFHW) with cased hole completion, respectively, are studied. In summary, the proposed works enable an accurate and physically valid tool for simulating the complex coupled flow in dual-porosity media and embedded conduits.

The rest of the paper is organized as follows. In section 2, we propose the dual-porosity-Stokes model by introducing the governing equations and the corresponding interface conditions. In section 3, the weak formulation is derived and the well-posedness of the model are analyzed. In section 4, the finite element method is presented and analyzed. In section 5, four numerical experiments are provided to validate the model and illustrate the features of both the model and the finite element method. In section 6, a short conclusion is provided.

2. Dual-porosity-Stokes model. For a simple illustration of the model problem, we use a composite domain, which consists of a dual-porosity subdomain Ω_d and the conduit subdomain Ω_c , to describe a dual-porosity-conduit system sketched in Figure 1. These two subdomains are nonoverlapping, i.e., $\Omega_d \cap \Omega_c = \emptyset$. $\partial\Omega_d$ and $\partial\Omega_c$ are the boundaries of Ω_d and Ω_c , respectively. Γ_{cd} is the interface between these two subdomains. Let $\Gamma_d = \partial\Omega_d/\Gamma_{cd}$ and $\Gamma_c = \partial\Omega_c/\Gamma_{cd}$. We also consider the time domain $[0, T]$ for the model.

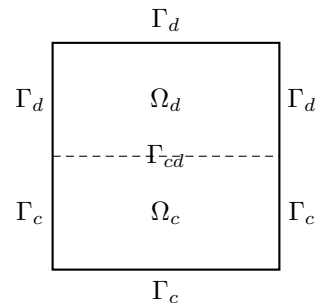


FIG. 1. The interface (dashed line) separates two subdomains: the dual-porosity media region and the free flow region.

In dual-porosity media, Ω_d , the dual-porosity model is used to govern the flow. First, we recall a traditional dual-porosity model, which is composed of matrix and microfracture equations [51, 88] as follows:

$$(2.1) \quad \phi_m C_{mt} \frac{\partial p_m}{\partial t} - \nabla \cdot \left(\frac{k_m}{\mu} \nabla p_m \right) = -Q,$$

$$(2.2) \quad \phi_f C_{ft} \frac{\partial p_f}{\partial t} - \nabla \cdot \left(\frac{k_f}{\mu} \nabla p_f \right) = Q + q_p,$$

where $Q = \frac{\sigma k_m}{\mu}(p_m - p_f)$ is a mass exchange term between matrix and microfractures, σ is a shape factor characterizing the morphology and dimension of the microfractures, ϕ_m (ϕ_f) denotes the porosity of the matrix (fracture) medium, C_{mt} (C_{ft}) is the total compressibility for the matrix (fracture) system, p_m (p_f) is the pressure in matrix (fracture), k_m (k_f) is the intrinsic permeability in matrix (fracture), μ is the dynamic viscosity, and q_p is the sink/source term.

In the conduits Ω_c , such as hydraulic fractures and horizontal wellbore, the flow is governed by the Stokes equation

$$(2.3) \quad \frac{\partial \mathbf{u}_c}{\partial t} - \nabla \cdot \mathbb{T}(\mathbf{u}_c, p) = \mathbf{f},$$

$$(2.4) \quad \nabla \cdot \mathbf{u}_c = 0,$$

where \mathbf{u}_c is the velocity, p is the kinematic pressure, $\mathbb{T}(\mathbf{u}_c, p) := 2\nu\mathbb{D}(\mathbf{u}_c) - p\mathbb{I}$ is the stress tensor, $\mathbb{D}(\mathbf{u}_c) := \frac{1}{2}(\nabla\mathbf{u}_c + \nabla\mathbf{u}_c^T)$ is the deformation tensor, \mathbb{I} is the identity matrix, ν is the kinematic viscosity of the fluid, and \mathbf{f} is a general body forcing term.

To combine the two separate models above together into the coupled system, we need to propose four interface conditions on the interface Γ_{cd} based on the following fundamental property of dual-porosity media. In general, the matrix permeability in a dual-porosity medium is critically low compared with the microfracture permeability. For example, in a shale or tight reservoir, the matrix permeability is usually 10^5 to 10^7 times smaller than the microfracture permeability [11, 12, 16, 24, 51]. On the other hand, the matrix porosity is usually 10^2 to 10^3 times larger than the microfracture porosity [12, 24, 51]. Furthermore, the shape factor σ , which ranges from 0 to 1, can be determined according to the morphology and dimension of the microfractures by using different types of formulas; see [64, 66, 71, 85] and the references therein for more details.

Therefore, in the dual-porosity media, the matrix system serves as the main storage space and the microfracture system serves as the preferential fluid movement channel. Due to the critically low permeability in the matrix and the much faster flow in the microfractures, the dual-porosity model neglects the flows between the matrix and the conduits/macrofractures. That is, the dual-porosity model assumes that the fluid drains from the matrix block into the adjacent microfractures and then into the conduits/macrofractures [9, 15, 48, 58, 60, 72]. Since the matrix is assumed to only feed the microfractures, the conduits/macrofractures do not directly communicate with the matrix but are only fed by the microfractures.

The first interface condition is a no-exchange condition between the matrix and the conduits/macrofractures:

$$(2.5) \quad -\frac{k_m}{\mu}\nabla p_m \cdot (-\mathbf{n}_{cd}) = 0,$$

where \mathbf{n}_{cd} is the unit normal vector on the interface edges pointing from Ω_c to Ω_d . The no-exchange condition means no flux could go across the interface from the matrix system directly to the conduits. This is based on the above fundamental property of the dual-porosity model which assumes that the matrix only feeds the microfractures and does not directly communicate with the conduits/macrofractures.

Then, similar to the three interface conditions of the Stokes–Darcy model, the following three conditions are imposed for the interaction between the flow in the microfractures and the flow in the conduits/macrofractures:

$$(2.6) \quad \mathbf{u}_c \cdot \mathbf{n}_{cd} = -\frac{k_f}{\mu}\nabla p_f \cdot \mathbf{n}_{cd},$$

$$(2.7) \quad -\mathbf{n}_{cd}^T \mathbb{T}(\mathbf{u}_c, p) \mathbf{n}_{cd} = \frac{p_f}{\rho},$$

$$(2.8) \quad -\mathbb{P}_\tau(\mathbb{T}(\mathbf{u}_c, p) \mathbf{n}_{cd}) = \frac{\alpha \nu \sqrt{N}}{\sqrt{\text{trace}(\mathbf{\Pi})}} \mathbb{P}_\tau \left(\mathbf{u}_c + \frac{k_f}{\mu} \nabla p_f \right),$$

where \mathbb{P}_τ denotes the projection onto the local tangent plane on Γ_{cd} , α is a constant parameter, $\mathbf{\Pi}$ is the intrinsic permeability of the fracture medium and $\mathbf{\Pi} = k_f \mathbb{I}$, N is the spatial dimension, and ρ is the fluid density. The interface condition (2.6) stands for the conservation of mass between the microfractures and the conduits. The condition (2.7) describes the balance of the forces [26, 31]. The last condition (2.8) is referred to as the Beavers–Joseph interface condition [10], which has been studied for the Stokes–Darcy model [20, 22, 23, 29, 41, 55]. These three conditions comply with the above fundamental property of the dual-porosity model. That is, the conduits/macrofractures are only fed by the microfractures, and the flux transfer and exchange on the interface only happens between the microfractures and the conduits/macrofractures.

For simplicity, we impose the following Dirichlet boundary conditions:

$$(2.9) \quad p_m = p_m^{dir}, \quad p_f = p_f^{dir} \text{ on } \Gamma_d; \quad \mathbf{u}_c = \mathbf{u}^{dir} \text{ on } \Gamma_c.$$

For real world applications, more realistic boundary conditions may need to be imposed, which will be discussed in the examples of section 5. The initial conditions for the problem are given by

$$(2.10) \quad p_m(\mathbf{x}, 0) = p_m^0, \quad p_f(\mathbf{x}, 0) = p_f^0, \quad \mathbf{u}_c(\mathbf{x}, 0) = \mathbf{u}_c^0.$$

3. Weak formulation. In this section, we will derive the weak formulation and show the well-posedness for the proposed model. Define the Hilbert spaces

$$\begin{aligned} H_{\Gamma_d}^s &:= \{\psi \in H^s(\Omega_d) : \psi = 0 \text{ on } \Gamma_d\}, \\ \mathbf{H}_{\Gamma_c}^s &:= \{\mathbf{v} \in [H^s(\Omega_c)]^N : \mathbf{v} = 0 \text{ on } \Gamma_c\}, \quad M := L^2(\Omega_c), \end{aligned}$$

and the product Hilbert spaces

$$\begin{aligned} \mathbf{X} &:= H^1(\Omega_d) \times H^1(\Omega_d) \times [H^1(\Omega_c)]^N, \\ \mathbf{X}_0 &:= H_{\Gamma_d}^1 \times H_{\Gamma_d}^1 \times \mathbf{H}_{\Gamma_c}^1, \quad \mathbf{L}^2 := L^2(\Omega_d) \times L^2(\Omega_d) \times [L^2(\Omega_c)]^N. \end{aligned}$$

Define two norms on M and \mathbf{X}_0 , respectively:

$$\begin{aligned} \|q\|_0 &:= \|q\|_M \quad \forall q \in M; \\ \|\vec{\mathbf{u}}\|_{\mathbf{X}_0} &:= \left(\|p_m\|_{H_{\Gamma_d}^1}^2 + \|p_f\|_{H_{\Gamma_d}^1}^2 + \|\mathbf{u}_c\|_{\mathbf{H}_{\Gamma_c}^1}^2 \right)^{1/2} \quad \forall \vec{\mathbf{u}} = (p_m, p_f, \mathbf{u}_c) \in \mathbf{X}_0. \end{aligned}$$

We also need the trace space defined as $\mathbf{H}_{00}^{\frac{1}{2}}(\Gamma_{cd}) := \mathbf{H}_{\Gamma_c}^1|_{\Gamma_{cd}}$, which is a nonclosed subspace of $\mathbf{H}^{\frac{1}{2}}(\Gamma_{cd})$ and has a continuous zero extension to $\mathbf{H}^{\frac{1}{2}}(\partial\Omega_c)$ [22, 23].

We briefly derive the weak formulation of the coupled dual-porosity-Stokes system from the two original models with interface conditions. First, multiplying the equations of dual-porosity model (2.1) and (2.2) by test functions ψ_m and ψ_f , respectively, and then integrating the result over Ω_d , we have, for all $(\psi_m, \psi_f) \in H_{\Gamma_d}^1 \times H_{\Gamma_d}^1$ and $t \in (0, T)$,

$$(3.1) \quad \int_{\Omega_d} \left(\phi_m C_{mt} \frac{\partial p_m}{\partial t} \psi_m + \frac{k_m}{\mu} \nabla p_m \cdot \nabla \psi_m + \frac{\sigma k_m}{\mu} (p_m - p_f) \psi_m \right) d\Omega - \int_{\Gamma_{cd}} \left(\frac{k_m}{\mu} \nabla p_m \cdot (-\mathbf{n}_{cd}) \right) \psi_m d\Gamma = 0,$$

$$(3.2) \quad \int_{\Omega_d} \left(\phi_f C_{ft} \frac{\partial p_f}{\partial t} \psi_f + \frac{k_f}{\mu} \nabla p_f \cdot \nabla \psi_f + \frac{\sigma k_m}{\mu} (p_f - p_m) \psi_f \right) d\Omega - \int_{\Gamma_{cd}} \left(\frac{k_f}{\mu} \nabla p_f \cdot (-\mathbf{n}_{cd}) \right) \psi_f d\Gamma = \int_{\Omega_d} q_p \psi_f d\Omega.$$

Similarly, multiplying the Stokes system (2.3) and (2.4) by a velocity test function \mathbf{v} and a pressure test function q , respectively, integrating the result over Ω_c , we have, for all $(\mathbf{v}, q) \in \mathbf{H}_{\Gamma_c}^1 \times M$ and $t \in (0, T)$,

$$(3.3) \quad \int_{\Omega_c} \left(\frac{\partial \mathbf{u}_c}{\partial t} \cdot \mathbf{v} + (2\nu \mathbb{D}(\mathbf{u}_c) - p\mathbb{I}) \cdot \nabla \mathbf{v} \right) d\Omega - \int_{\Gamma_{cd}} \left(\mathbf{n}_{cd}^T (2\nu \mathbb{D}(\mathbf{u}_c) - p\mathbb{I}) \mathbf{n}_{cd} \right) \mathbf{v} \cdot \mathbf{n}_{cd} d\Gamma - \int_{\Gamma_{cd}} \mathbb{P}_\tau((2\nu \mathbb{D}(\mathbf{u}_c) - p\mathbb{I}) \mathbf{n}_{cd}) \cdot \mathbf{v} d\Gamma = \int_{\Omega_c} \mathbf{f} \cdot \mathbf{v} d\Omega,$$

$$(3.4) \quad \int_{\Omega_c} (\nabla \cdot \mathbf{u}_c) q d\Omega = 0.$$

Next, to couple the two subsystems (3.1)–(3.2) and (3.3)–(3.4) into the complete system, we apply the interface condition (2.5) to (3.1), apply the interface condition (2.6) to (3.2), and apply the interface conditions (2.7)–(2.8) to (3.3). Then, multiplying (3.3)–(3.4) by a rescaling constant η and summing all the resulting equations, we obtain

$$(3.5) \quad \int_{\Omega_d} \left(\phi_m C_{mt} \frac{\partial p_m}{\partial t} \psi_m + \frac{k_m}{\mu} \nabla p_m \cdot \nabla \psi_m + \frac{\sigma k_m}{\mu} (p_m - p_f) \psi_m \right) d\Omega + \int_{\Omega_d} \left(\phi_f C_{ft} \frac{\partial p_f}{\partial t} \psi_f + \frac{k_f}{\mu} \nabla p_f \cdot \nabla \psi_f + \frac{\sigma k_m}{\mu} (p_f - p_m) \psi_f \right) d\Omega - \int_{\Gamma_{cd}} \mathbf{u}_c \cdot \mathbf{n}_{cd} \psi_f d\Gamma + \eta \int_{\Omega_c} \left(\frac{\partial \mathbf{u}_c}{\partial t} \cdot \mathbf{v} + 2\nu \mathbb{D}(\mathbf{u}_c) : \mathbb{D}(\mathbf{v}) - p \nabla \cdot \mathbf{v} \right) d\Omega + \eta \int_{\Gamma_{cd}} \left(\frac{1}{\rho} p_f \mathbf{v} \cdot \mathbf{n}_{cd} + \frac{\alpha \nu \sqrt{N}}{\sqrt{\text{trace}(\mathbb{II})}} \mathbb{P}_\tau \left(\mathbf{u}_c + \frac{k_f}{\mu} \nabla p_f \right) \cdot \mathbf{v} \right) d\Gamma = \eta \int_{\Omega_c} \mathbf{f} \cdot \mathbf{v} d\Omega + \int_{\Omega_d} q_p \psi_f d\Omega,$$

$$(3.6) \quad \eta \int_{\Omega_c} \nabla \cdot \mathbf{u}_c q d\Omega = 0.$$

Here the integral of $\mathbb{P}_\tau(\frac{k_f}{\mu} \nabla p_f) \cdot \mathbf{v}$ on Γ_{cd} is understood to be the value of the functional $\mathbb{P}_\tau(\frac{k_f}{\mu} \nabla p_f)|_{\Gamma_{cd}} \in (\mathbf{H}_{00}^{\frac{1}{2}}(\Gamma_{cd}))'$ applied to $\mathbf{v}|_{\Gamma_{cd}} \in \mathbf{H}_{00}^{\frac{1}{2}}(\Gamma_{cd})$, which is well defined when k_f is isotropic; see [23] and the references cited therein.

For simplicity, we define the bilinear forms $a_\eta(\cdot, \cdot) : \mathbf{X}_0 \times \mathbf{X}_0 \rightarrow \mathbb{R}$ and $b_\eta(\cdot, \cdot) : M \times \mathbf{X}_0 \rightarrow \mathbb{R}$ as follows. For $\vec{\mathbf{u}} = (p_m, p_f, \mathbf{u}_c)$ and $\vec{\mathbf{v}} = (\psi_m, \psi_f, \mathbf{v})$ in \mathbf{X}_0 and p in

M , define

$$\begin{aligned}
 a_\eta(\vec{\mathbf{u}}, \vec{\mathbf{v}}) &= \int_{\Omega_d} \left(\frac{k_m}{\mu} \nabla p_m \cdot \nabla \psi_m + \frac{\sigma k_m}{\mu} (p_m - p_f) \psi_m \right) d\Omega \\
 &\quad + \int_{\Omega_d} \left(\frac{k_f}{\mu} \nabla p_f \cdot \nabla \psi_f + \frac{\sigma k_m}{\mu} (p_f - p_m) \psi_f \right) d\Omega \\
 &\quad + \int_{\Gamma_{cd}} (-\mathbf{u}_c \cdot \mathbf{n}_{cd} \psi_f + \frac{\eta}{\rho} p_f \mathbf{v} \cdot \mathbf{n}_{cd}) d\Gamma + \eta \int_{\Omega_c} 2\nu \mathbb{D}(\mathbf{u}_c) : \mathbb{D}(\mathbf{v}) d\Omega \\
 (3.7) \quad &\quad + \eta \int_{\Gamma_{cd}} \left(\frac{\alpha \nu \sqrt{N}}{\sqrt{\text{trace}(\mathbf{\Pi})}} \mathbb{P}_\tau(\mathbf{u}_c + \frac{k_f}{\mu} \nabla p_f) \cdot \mathbf{v} \right) d\Gamma
 \end{aligned}$$

and

$$(3.8) \quad b_\eta(p, \mathbf{v}) = -\eta \int_{\Omega_c} p \nabla \cdot \mathbf{v} d\Omega.$$

We also define the inner product $\langle \cdot, \cdot \rangle_\eta : \mathbf{X}_0 \times \mathbf{X}_0 \rightarrow \mathbb{R}$

$$(3.9) \quad \langle \partial_t \vec{\mathbf{u}}, \vec{\mathbf{v}} \rangle_\eta = \int_{\Omega_d} \left(\phi_m C_{mt} \frac{\partial p_m}{\partial t} \psi_m + \phi_f C_{ft} \frac{\partial p_f}{\partial t} \psi_f \right) d\Omega + \eta \int_{\Omega_c} \frac{\partial \mathbf{u}_c}{\partial t} \cdot \mathbf{v} d\Omega$$

and the linear forcing functional $\ell_\eta(\cdot) : \mathbf{X}_0 \rightarrow \mathbb{R}$

$$(3.10) \quad \ell_\eta(\vec{\mathbf{v}}) = \begin{pmatrix} \mathbf{0} \\ \eta \langle \mathbf{f}, \mathbf{v} \rangle_{\Omega_c} + \langle q_p, \psi_f \rangle_{\Omega_d} \end{pmatrix},$$

where $\langle \mathbf{f}, \mathbf{v} \rangle_{\Omega_c} := \int_{\Omega_c} \mathbf{f} \cdot \mathbf{v} d\Omega$ and $\langle q_p, \psi_f \rangle_{\Omega_d} := \int_{\Omega_d} q_p \psi_f d\Omega$ are the dualities induced by the L^2 inner product on Ω_c and Ω_d , respectively.

Thus, the weak formulation is to find $(\vec{\mathbf{u}}, p) = (p_m, p_f, \mathbf{u}_c, p) \in L^2(0, T; \mathbf{X}_0) \times L^2(0, T; M)$ such that

$$(3.11) \quad \langle \partial_t \vec{\mathbf{u}}, \vec{\mathbf{v}} \rangle_\eta + a_\eta(\vec{\mathbf{u}}, \vec{\mathbf{v}}) + b_\eta(p, \mathbf{v}) = \ell_\eta(\vec{\mathbf{v}}) \quad \forall \vec{\mathbf{v}} = (\psi_m, \psi_f, \mathbf{v}) \in \mathbf{X}_0,$$

$$(3.12) \quad b_\eta(q, \mathbf{u}_c) = 0 \quad \forall q \in M$$

with the initial condition $\vec{\mathbf{u}}(0) = \vec{\mathbf{u}}_0$, where $\partial_t \vec{\mathbf{u}} \in H^1(0, T; \mathbf{X}'_0)$, \mathbf{X}'_0 denotes the dual space of \mathbf{X}_0 , and $\vec{\mathbf{u}}_0 = (p_m^0, p_f^0, \mathbf{u}_c^0)$. For the general Dirichlet boundary condition (2.9), the standard homogenization technique can be applied to obtain an equivalent system with the homogeneous Dirichlet boundary conditions.

In the rest of this section, we will follow the analysis in [23] to show the continuity and a Gårding-type inequality of $a_\eta(\cdot, \cdot)$ for the well-posedness of the proposed model. For simplification, we will use $\|\cdot\|_1$ to denote the H^1 norm of the corresponding space and $\|\cdot\|_0$ to denote the L^2 norm of the corresponding space. First, we have the following lemma for the continuity of $a_\eta(\cdot, \cdot)$.

LEMMA 1. *The bilinear form $a_\eta(\cdot, \cdot)$ is continuous on \mathbf{X}_0 ; i.e., there exists a constant C_η such that, for all $\vec{\mathbf{u}}, \vec{\mathbf{v}} \in \mathbf{X}_0$,*

$$(3.13) \quad a_\eta(\vec{\mathbf{u}}, \vec{\mathbf{v}}) \leq C_\eta \|\vec{\mathbf{u}}\|_{\mathbf{X}_0} \|\vec{\mathbf{v}}\|_{\mathbf{X}_0}.$$

Proof. Using the Cauchy–Schwarz inequality, the trace inequality, and Poincaré inequality, we have

$$\begin{aligned}
 a_\eta(\vec{\mathbf{u}}, \vec{\mathbf{v}}) &\leq \left| \frac{k_m}{\mu} \right| \|p_m\|_1 \|\psi_m\|_1 + \left| \frac{k_f + \sigma k_m}{\mu} \right| \|p_f\|_1 \|\psi_f\|_1 + |2\eta\nu| \|\mathbf{u}_c\|_1 \|\mathbf{v}\|_1 \\
 &\quad + \left| \frac{\sigma k_m}{\mu} \right| \|p_m\|_1 \|\psi_m\|_1 + \left| \frac{C_4 \sqrt{N} \eta \nu \alpha}{\sqrt{\lambda_{\min}(\mathbf{\Pi})}} + \frac{\eta}{\rho} C_2 \right| \|p_f\|_1 \|\mathbf{v}\|_1 + C_1 \|\mathbf{u}_c\|_1 \|\psi_f\|_1 \\
 (3.14) \quad &\quad + \left| \frac{\sigma k_m}{\mu} \right| \|p_m\|_1 \|\psi_f\|_1 + \left| \frac{\sigma k_m}{\mu} \right| \|p_f\|_1 \|\psi_m\|_1 + \left| \frac{C_3 \sqrt{N} \eta \nu \alpha}{\sqrt{\lambda_{\min}(\mathbf{\Pi})}} \right| \|\mathbf{u}_c\|_1 \|\mathbf{v}\|_1,
 \end{aligned}$$

where the C_i 's are generic constants depending on the domain and the interface and $\lambda_{\min}(\mathbf{\Pi})$ denotes the smallest eigenvalues of $\mathbf{\Pi}$. Define

$$\begin{aligned}
 \gamma_{1,\eta} &= \max \left\{ \left| \frac{k_m}{\mu} \right|, \left| \frac{k_f + \sigma k_m}{\mu} \right|, |2\eta\nu| \right\}, \quad \gamma_{2,\eta} = \max \left\{ \left| \frac{\sigma k_m}{\mu} \right|, \left| \frac{C_4 \sqrt{N} \eta \nu \alpha}{\sqrt{\lambda_{\min}(\mathbf{\Pi})}} + \frac{\eta}{\rho} C_2 \right|, C_1 \right\}, \\
 \gamma_{3,\eta} &= \max \left\{ \left| \frac{\sigma k_m}{\mu} \right|, \left| \frac{C_3 \sqrt{N} \eta \nu \alpha}{\sqrt{\lambda_{\min}(\mathbf{\Pi})}} \right| \right\}, \quad C_\eta = \max\{\gamma_{1,\eta}, \gamma_{2,\eta}, \gamma_{3,\eta}\}.
 \end{aligned}$$

Then the inequality (3.14) leads to

$$\begin{aligned}
 a_\eta(\vec{\mathbf{u}}, \vec{\mathbf{v}}) &\leq \gamma_{1,\eta} (\|p_m\|_1^2 + \|p_f\|_1^2 + \|\mathbf{u}_c\|_1^2)^{1/2} (\|\psi_m\|_1^2 + \|\psi_f\|_1^2 + \|\mathbf{v}\|_1^2)^{1/2} \\
 &\quad + \gamma_{2,\eta} (\|p_m\|_1^2 + \|p_f\|_1^2 + \|\mathbf{u}_c\|_1^2)^{1/2} (\|\psi_m\|_1^2 + \|\psi_f\|_1^2 + \|\mathbf{v}\|_1^2)^{1/2} \\
 &\quad + \gamma_{3,\eta} (\|p_m\|_1^2 + \|p_f\|_1^2 + \|\mathbf{u}_c\|_1^2)^{1/2} (\|\psi_m\|_1^2 + \|\psi_f\|_1^2 + \|\mathbf{v}\|_1^2)^{1/2} \\
 (3.15) \quad &= C_\eta \|\vec{\mathbf{u}}\|_{\mathbf{X}_0} \|\vec{\mathbf{v}}\|_{\mathbf{X}_0},
 \end{aligned}$$

which completes the proof of the continuity of the bilinear form $a_\eta(\cdot, \cdot)$. \square

In the following lemma, we will follow the idea in [23] to show that the bilinear form $a_\eta(\cdot, \cdot)$ is essentially coercive in the sense of a Gårding-type inequality [44].

LEMMA 2. *The bilinear form $a_\eta(\cdot, \cdot)$ satisfies the following Gårding-type inequality: for small enough rescaling parameter $\eta > 0$, there exist constants $C_{1,\eta} > 0$ and $C_{0,\eta} > 0$ such that*

$$(3.16) \quad a_\eta(\vec{\mathbf{u}}, \vec{\mathbf{u}}) \geq C_{1,\eta} \|\vec{\mathbf{u}}\|_{\mathbf{X}_0}^2 - C_{0,\eta} \|\vec{\mathbf{u}}\|_{\mathbf{L}^2}^2 \quad \forall \vec{\mathbf{u}} \in \mathbf{X}_0.$$

Proof. According to the Cauchy–Schwarz, Korn’s, the Poincaré, the trace, and Young’s inequalities, we obtain

$$\begin{aligned}
 (3.17) \quad &a_\eta(\vec{\mathbf{u}}, \vec{\mathbf{u}}) + C_{0,\eta} \|\vec{\mathbf{u}}\|_{\mathbf{L}^2}^2 \\
 &= C_{0,\eta} \|\vec{\mathbf{u}}\|_{\mathbf{L}^2}^2 + 2\eta\nu \|\mathbb{D}(\mathbf{u}_c)\|_0^2 + \frac{1}{\mu} \int_{\Omega_d} k_m \nabla p_m \cdot \nabla p_m d\Omega_d + \frac{\sigma}{\mu} \int_{\Omega_d} k_m (p_m - p_f)^2 d\Omega_d \\
 &\quad + \frac{1}{\mu} \int_{\Omega_d} k_f \nabla p_f \cdot \nabla p_f d\Omega_d + \left(\frac{\eta}{\rho} - 1 \right) \int_{\Gamma_{cd}} p_f \mathbf{u}_c \cdot \mathbf{n}_{cd} d\Gamma + \frac{\sqrt{N} \eta \alpha \nu}{\sqrt{k_f}} \left\| \mathbb{P}_\tau(\mathbf{u}_c) \right\|_{L^2(\Gamma_{cd})}^2 \\
 &\quad + \left\langle \frac{\eta \alpha \nu \sqrt{N} k_f}{\mu} \mathbb{P}_\tau(\nabla p_f), \mathbb{P}_\tau(\mathbf{u}_c) \right\rangle_{((\mathbf{H}_{00}^{1/2}(\Gamma_{cd}))', \mathbf{H}_{00}^{1/2}(\Gamma_{cd}))} \\
 &\geq C_{0,\eta} \|p_m\|_0^2 + C_{0,\eta} \|p_f\|_0^2 + C_{0,\eta} \|\mathbf{u}_c\|_0^2 + \frac{k_m}{\mu} \|\nabla p_m\|_0^2 + \frac{k_f}{\mu} \|\nabla p_f\|_0^2 + 2\eta\nu C_5 \|\nabla \mathbf{u}_c\|_0^2 \\
 &\quad - \left(1 + \frac{\eta}{\rho} \right) C_6 \|p_f\|_0^{\frac{1}{2}} \|\mathbf{u}_c\|_0^{\frac{1}{2}} \|\nabla p_f\|_0^{\frac{1}{2}} \|\nabla \mathbf{u}_c\|_0^{\frac{1}{2}} - \frac{\sqrt{N} k_f \eta \alpha \nu}{\mu} C_7 \|\nabla p_f\|_0 \|\nabla \mathbf{u}_c\|_0
 \end{aligned}$$

$$\begin{aligned}
 &\geq C_{0,\eta} \|p_m\|_0^2 + C_{0,\eta} \|p_f\|_0^2 + C_{0,\eta} \|\mathbf{u}_c\|_0^2 + \frac{k_m}{\mu} \|\nabla p_m\|_0^2 + \frac{k_f}{\mu} \|\nabla p_f\|_0^2 + 2\eta\nu C_5 \|\nabla \mathbf{u}_c\|_0^2 \\
 &\quad - \frac{\eta\nu C_5}{2} \|\nabla \mathbf{u}_c\|_0^2 - \frac{k_f}{4\mu} \|\nabla p_f\|_0^2 - \frac{\sqrt{\mu}(1 + \frac{\eta}{\rho})^2 C_2^2}{2\sqrt{\eta\nu C_5 k_f}} \|p_f\|_0^2 - \frac{\sqrt{\mu}(1 + \frac{\eta}{\rho})^2 C_2^2}{2\sqrt{\eta\nu C_5 k_f}} \|\mathbf{u}_c\|_0^2 \\
 &\quad - \frac{\eta\nu C_5}{2} \|\nabla \mathbf{u}_c\|_0^2 - \frac{Nk_f \eta \alpha^2 \nu}{2C_5 \mu^2} \|\nabla p_f\|_0^2 \\
 &\geq C_{1,\eta} \|\vec{\mathbf{u}}\|_{X_0}^2,
 \end{aligned}$$

where the C_i 's are generic constants depending on the domain and interface, $C_{1,\eta} = \min\{\frac{C_{0,\eta}}{2}, \eta\nu C_5, \frac{k_m}{2\mu}, \frac{k_f}{\mu}\}$, and we choose small enough rescaling parameter η and large enough $C_{0,\eta}$ such that

$$\frac{Nk_f \eta \alpha^2 \nu}{2C_5 \mu^2} \leq \frac{k_f}{4\mu}, \quad \frac{\sqrt{\mu}(1 + \frac{\eta}{\rho})^2 C_2^2}{\sqrt{\eta\nu C_5 k_f}} \leq C_{0,\eta}.$$

This completes the proof of Lemma 2. □

Combining Lemmas 1 and 2 and Lemma 3.1 of [23], we can obtain the following well-posedness conclusion.

THEOREM 3. *The dual-porosity-Stokes model with the four interface conditions (2.5)–(2.8) is well-posed.*

4. Finite element method. Let $\mathbf{X}_0^h = H_{\Gamma_d}^h \times H_{\Gamma_d}^h \times \mathbf{H}_{\Gamma_c}^h$ and M^h be proper finite element subspaces of $\mathbf{X}_0 = H_{\Gamma_d}^1 \times H_{\Gamma_d}^1 \times \mathbf{H}_{\Gamma_c}^1$ and M , respectively. The pair \mathbf{X}_0^h and M^h is assumed to satisfy the discrete inf-sup condition, that is, there exists a constant $\beta > 0$ such that

$$(4.1) \quad \inf_{0 \neq q_h \in M^h} \sup_{0 \neq \mathbf{v}_h \in \mathbf{H}_{\Gamma_c}^h} \frac{b_\eta(q_h, \mathbf{v}_h)}{\|q_h\|_0 \|\mathbf{v}_h\|_1} \geq \beta.$$

Consider \mathbf{X}_0^h with continuous piecewise polynomials of degree k and M^h with continuous piecewise polynomials of degree $k - 1$ ($k \geq 1$). First, we assume that the subspaces \mathbf{X}_0^h and M^h satisfy the following approximation properties:

$$(4.2) \quad \inf_{\vec{\mathbf{v}}_h \in \mathbf{X}_0^h} \|\vec{\mathbf{v}} - \vec{\mathbf{v}}_h\|_1 \leq Ch^r \|\vec{\mathbf{v}}\|_{r+1} \quad \forall \vec{\mathbf{v}} \in H_{\Gamma_d}^{r+1} \times H_{\Gamma_d}^{r+1} \times \mathbf{H}_{\Gamma_c}^{r+1}, \quad 0 < r \leq k,$$

$$(4.3) \quad \inf_{q_h \in M^h} \|q - q_h\|_0 \leq Ch^r \|q\|_r \quad \forall q \in \mathbf{H}^r(\Omega_c), \quad 0 < r \leq k,$$

and the following projection properties:

$$(4.4) \quad \Pi^h \mathbf{w} \in H_{\Gamma_c}^h, (\nabla(\mathbf{w} - \Pi^h \mathbf{w}), q_h) = 0 \quad \forall q_h \in M^h, \mathbf{w} \in \mathbf{H}_{\Gamma_c}^1,$$

$$(4.5) \quad \|\mathbf{w} - \Pi^h \mathbf{w}\|_1 \leq Ch^s \|\mathbf{w}\|_{s+1} \quad \forall \mathbf{w} \in \mathbf{H}_{\Gamma_c}^{s+1},$$

where $\Pi^h : \mathbf{H}_{\Gamma_c}^1 \rightarrow \mathbf{H}_{\Gamma_c}^h$ is a projection operator on subspaces \mathbf{X}_0^h and M^h , $0 \leq s \leq k$, and C is a positive constant independent of h and \mathbf{w} .

We also introduce the divergence-free function space

$$(4.6) \quad \mathbf{X}_0^{\text{div}} = H_{\Gamma_d}^1 \times H_{\Gamma_d}^1 \times \mathbf{H}_{\Gamma_c, \text{div}}^1, \quad \text{where } H_{\Gamma_c, \text{div}}^1 = \{\mathbf{w} \in \mathbf{H}_{\Gamma_c}^1 \mid \text{div } \mathbf{w} = 0\},$$

and the discretely divergence-free finite element space

$$(4.7) \quad \mathbf{X}_0^{h, \text{div}} = \{(\psi_m, \psi_f, \mathbf{v}) \in \mathbf{X}_0^h : b(\mathbf{v}_h, q_h) = 0 \quad \forall q_h \in M^h\}.$$

Define $\mathcal{P}^h : \mathbf{L}^2 \rightarrow \mathbf{X}_0^{h,\text{div}}$ to be the projection operator with respect to the \mathbf{L}^2 inner product, i.e.,

$$(4.8) \quad \mathcal{P}^h \vec{\mathbf{z}} \in \mathbf{X}_0^{h,\text{div}}, (\mathcal{P}^h \vec{\mathbf{z}}, \vec{\mathbf{v}}_h) = (\vec{\mathbf{z}}, \vec{\mathbf{v}}_h) \quad \forall \vec{\mathbf{v}}_h \in \mathbf{X}_0^{h,\text{div}}, \vec{\mathbf{z}} \in \mathbf{L}^2.$$

We recall that the operator \mathcal{P}^h satisfies the following approximation properties (see Propositions 2.2 and 2.6 in [57]):

$$(4.9) \quad \|\vec{\mathbf{z}} - \mathcal{P}^h \vec{\mathbf{z}}\|_1 \rightarrow 0 \text{ as } h \rightarrow 0 \quad \forall \vec{\mathbf{z}} \in \mathbf{X}_0^{\text{div}};$$

$$(4.10) \quad \|\vec{\mathbf{z}} - \mathcal{P}^h \vec{\mathbf{z}}\|_1 \leq Ch^r \|\vec{\mathbf{z}}\|_{r+1} \quad \forall \vec{\mathbf{z}} \in H_{\Gamma_d}^{r+1} \times H_{\Gamma_d}^{r+1} \times \mathbf{H}_{\Gamma_c}^{r+1} \cap \mathbf{X}_0^{\text{div}};$$

$$(4.11) \quad \|\vec{\mathbf{z}} - \mathcal{P}^h \vec{\mathbf{z}}\|_0 \leq Ch^{r+1} \|\vec{\mathbf{z}}\|_{r+1} \quad \forall \vec{\mathbf{z}} \in H_{\Gamma_d}^{r+1} \times H_{\Gamma_d}^{r+1} \times \mathbf{H}_{\Gamma_c}^{r+1} \cap \mathbf{X}_0^{\text{div}};$$

$$(4.12) \quad \|\vec{\mathbf{z}} - \mathcal{P}^h \vec{\mathbf{z}}\|_{L^2(0,T;\mathbf{X}_0)} \rightarrow 0 \text{ as } h \rightarrow 0 \quad \forall \vec{\mathbf{z}} \in L^2(0,T;\mathbf{X}_0^{\text{div}});$$

$$(4.13) \quad \|\vec{\mathbf{z}} - \mathcal{P}^h \vec{\mathbf{z}}\|_{L^2(0,T;\mathbf{X}_0)} \leq Ch^r \|\vec{\mathbf{z}}\|_{L^2(0,T;H_{\Gamma_d}^{r+1} \times H_{\Gamma_d}^{r+1} \times \mathbf{H}_{\Gamma_c}^{r+1})} \\ \forall \vec{\mathbf{z}} \in L^2(0,T;H_{\Gamma_d}^{r+1} \times H_{\Gamma_d}^{r+1} \times \mathbf{H}_{\Gamma_c}^{r+1} \cap \mathbf{X}_0^{\text{div}});$$

$$(4.14) \quad \|\vec{\mathbf{z}} - \mathcal{P}^h \vec{\mathbf{z}}\|_{L^2(0,T;M)} \leq Ch^{r+1} \|\vec{\mathbf{z}}\|_{L^2(0,T;H_{\Gamma_d}^{r+1} \times H_{\Gamma_d}^{r+1} \times \mathbf{H}_{\Gamma_c}^{r+1})} \\ \forall \vec{\mathbf{z}} \in L^2(0,T;H_{\Gamma_d}^{r+1} \times H_{\Gamma_d}^{r+1} \times \mathbf{H}_{\Gamma_c}^{r+1} \cap \mathbf{X}_0^{\text{div}}),$$

where $r \in [0, k]$.

4.1. Discretization. The finite element semidiscretization for (3.11)–(3.12) is to find $(\vec{\mathbf{u}}_h, p_h) = (p_{mh}, p_{fh}, \mathbf{u}_{ch}, p_h) \in H^1(0, T; \mathbf{X}_0^h) \times L^2(0, T; M^h)$ satisfying

$$(4.15) \quad \langle \partial_t \vec{\mathbf{u}}_h, \vec{\mathbf{v}}_h \rangle_\eta + a_\eta(\vec{\mathbf{u}}_h, \vec{\mathbf{v}}_h) + b_\eta(p_h, \mathbf{v}_h) = \ell_\eta(\vec{\mathbf{v}}_h) \\ \forall \vec{\mathbf{v}}_h = (\psi_{mh}, \psi_{fh}, \mathbf{v}_h) \in \mathbf{X}_0^h,$$

$$(4.16) \quad b_\eta(q_h, \mathbf{u}_{ch}) = 0 \quad \forall q_h \in M^h,$$

together with the initial condition $\vec{\mathbf{u}}_h(0) = \mathcal{P}^h \vec{\mathbf{u}}_0$ and boundary condition $\vec{\mathbf{u}}_h = \mathcal{P}^h \vec{\mathbf{u}}_\Gamma$.

Based on the Gårding-type inequality (3.16) and the same argument in [22], it is easy to see that if the linear forcing functional $\ell_\eta \in L^2(0, T; \mathbf{L}^2)$, then the system (4.15)–(4.16) has a unique solution $(\vec{\mathbf{u}}_h, p_h) \in H^1(0, T; \mathbf{X}_0^{h,\text{div}}) \times L^2(0, T; M^h)$.

For the full discretization, we use Δt to denote the time step size and n to indicate the n th step at time $t_n = n\Delta t$. We first traditionally consider the backward Euler scheme as follows:

$$(4.17) \quad \left\langle \frac{\vec{\mathbf{u}}_h^n - \vec{\mathbf{u}}_h^{n-1}}{\Delta t}, \vec{\mathbf{v}}_h \right\rangle_\eta + a_\eta(\vec{\mathbf{u}}_h^n, \vec{\mathbf{v}}_h) + b_\eta(p_h^n, \mathbf{v}_h) = \ell_\eta^n(\vec{\mathbf{v}}_h),$$

$$(4.18) \quad b_\eta(q_h, \mathbf{u}_{ch}^n) = 0,$$

where

$$(4.19) \quad \ell_\eta^n(\vec{\mathbf{v}}_h) = \begin{pmatrix} \mathbf{0} \\ \eta \int_{\Omega_c} \mathbf{f}(t_n) \cdot \mathbf{v}_h d\Omega + \int_{\Omega_d} q_p(t_n) \psi_{fh} d\Omega \end{pmatrix}.$$

Since the backward Euler scheme has only first order accuracy, we also consider the Crank–Nicolson scheme, which has second order accuracy:

$$\begin{aligned}
 & \frac{1}{\Delta t} \langle \vec{\mathbf{u}}_h^n, \vec{\mathbf{v}}_h \rangle_\eta + \frac{1}{2} \left(a_\eta(\vec{\mathbf{u}}_h^n, \vec{\mathbf{v}}_h) + b_\eta(p_h^n, \mathbf{v}_h) + b_\eta(q_h, \mathbf{u}_{ch}^n) \right) \\
 &= -\frac{1}{2} \left(a_\eta(\vec{\mathbf{u}}_h^{n-1}, \vec{\mathbf{v}}_h) + b_\eta(p_h^{n-1}, \mathbf{v}_h) + b_\eta(q_h, \mathbf{u}_{ch}^{n-1}) \right) \\
 (4.20) \quad & + \frac{1}{2} \ell_\eta^n(\vec{\mathbf{v}}_h) + \frac{1}{2} \ell_\eta^{n-1}(\vec{\mathbf{v}}_h) + \frac{1}{\Delta t} \langle \vec{\mathbf{u}}_h^{n-1}, \vec{\mathbf{v}}_h \rangle_\eta.
 \end{aligned}$$

Both of the schemes above are single-step ones with unconditional stability. In the following, we consider two multistep schemes with unconditional stability. One scheme is the two-step backward differentiation scheme, which also has second order accuracy:

$$\begin{aligned}
 & \frac{1}{\Delta t} \left\langle \frac{3}{2} \vec{\mathbf{u}}_h^n, \vec{\mathbf{v}}_h \right\rangle_\eta + a_\eta(\vec{\mathbf{u}}_h^n, \vec{\mathbf{v}}_h) + b_\eta(p_h^n, \mathbf{v}_h) + b_\eta(q_h, \mathbf{u}_{ch}^n) \\
 (4.21) \quad &= \ell_\eta^n(\vec{\mathbf{v}}_h) + \frac{1}{\Delta t} \left\langle 2 \vec{\mathbf{u}}_h^{n-1} - \frac{1}{2} \vec{\mathbf{u}}_h^{n-2}, \vec{\mathbf{v}}_h \right\rangle_\eta.
 \end{aligned}$$

In addition to the original initial condition of the problem, this scheme needs an additional initial condition at the time step $n = 1$, which can be provided by the backward Euler scheme.

The other multistep scheme we consider is the three-step backward differentiation scheme, which has third order accuracy:

$$\begin{aligned}
 & \frac{1}{\Delta t} \left\langle \frac{11}{6} \vec{\mathbf{u}}_h^n, \vec{\mathbf{v}}_h \right\rangle_\eta + a_\eta(\vec{\mathbf{u}}_h^n, \vec{\mathbf{v}}_h) + b_\eta(p_h^n, \mathbf{v}_h) + b_\eta(q_h, \mathbf{u}_{ch}^n) \\
 (4.22) \quad &= \ell_\eta^n(\vec{\mathbf{v}}_h) + \frac{1}{\Delta t} \left\langle 3 \vec{\mathbf{u}}_h^{n-1} - \frac{3}{2} \vec{\mathbf{u}}_h^{n-2} + \frac{1}{3} \vec{\mathbf{u}}_h^{n-3}, \vec{\mathbf{v}}_h \right\rangle_\eta.
 \end{aligned}$$

In addition to the original initial condition of the problem, this scheme needs two additional initial conditions at the time steps $n = 1$ and $n = 2$, which can be provided by the Crank–Nicolson scheme and two-step backward differentiation scheme. When we use Taylor–Hood elements for the free flow and quadratic finite elements for the dual-porosity flow in the semidiscretization, we can reach third order accuracy in the L^2 norm. Then the three-step backward differentiation scheme can provide a global third order accuracy with $\Delta t = h$, while the backward Euler scheme needs $\Delta t = h^3$ for the same goal.

4.2. Convergence analysis. In this subsection, we will follow the analysis in [22] to show the convergence of full discretization with the backward Euler scheme. We first will introduce a projection operator which is similar to that of [22]. Define $\mathbb{P} = (\mathbb{P}_s \vec{\mathbf{u}}, \mathbb{P}_p p) : \mathbf{X}_0 \times M \rightarrow \mathbf{X}_0^h \times M^h$ such that, for $(\vec{\mathbf{u}}, p) \in \mathbf{X}_0 \times M$, the projection $(\mathbb{P}_s \vec{\mathbf{u}}, \mathbb{P}_p p) = (\mathbb{P}_{s1} p_m, \mathbb{P}_{s2} p_f, \mathbb{P}_{s3} \mathbf{u}_c, \mathbb{P}_p p)$ satisfies

$$(4.23) \quad a_\eta(\vec{\mathbf{u}} - \mathbb{P}_s \vec{\mathbf{u}}, \vec{\mathbf{v}}_h) + C_{0,\eta} \langle \vec{\mathbf{u}} - \mathbb{P}_s \vec{\mathbf{u}}, \vec{\mathbf{v}}_h \rangle_\eta + b_\eta(p - \mathbb{P}_p p, \mathbf{v}_h) = 0$$

$$(4.24) \quad \forall \vec{\mathbf{v}}_h = (\psi_{mh}, \psi_{fh}, \mathbf{v}) \in \mathbf{X}_0^h,$$

$$(4.24) \quad b_\eta(q_h, \mathbf{u}_c - \mathbb{P}_{s3} \mathbf{u}_c) = 0 \quad \forall q_h \in M^h.$$

There exists a unique solution $(\mathbb{P}_s \vec{\mathbf{u}}, \mathbb{P}_p p) \in \mathbf{X}_0^h \times M^h$ for a given $(\vec{\mathbf{u}}, p) \in \mathbf{X}_0 \times M$ according to the Gårding-type inequality (3.16), and the solution $(\mathbb{P}_s \vec{\mathbf{u}}, \mathbb{P}_p p)$ satisfies the following approximate properties.

LEMMA 4. Consider $0 < r \leq k$. Assume that

$$(\vec{\mathbf{u}}, p) = (p_m, p_f, \mathbf{u}_c, p) \in L^q(0, T; H_{\Gamma_d}^{r+1} \times H_{\Gamma_d}^{r+1} \times \mathbf{H}_{\Gamma_c}^{r+1}) \times L^q(0, T; \mathbf{H}^r(\Omega_c))$$

for some $q \in [1, \infty)$. Let $(\mathbb{P}_s \vec{\mathbf{u}}, \mathbb{P}_p p)$ be the projection solution of (4.23)–(4.24); then we have

$$(4.25) \quad \begin{aligned} & \|\vec{\mathbf{u}} - \mathbb{P}_s \vec{\mathbf{u}}\|_{L^q(0, T; H_{\Gamma_d}^1 \times H_{\Gamma_d}^1 \times \mathbf{H}_{\Gamma_c}^1)} + \|p - \mathbb{P}_p p\|_{L^q(0, T; M)} \\ & \leq Ch^r \left(\|\vec{\mathbf{u}}\|_{L^q(0, T; H_{\Gamma_d}^{r+1} \times H_{\Gamma_d}^{r+1} \times \mathbf{H}_{\Gamma_c}^{r+1})} + \|p\|_{L^q(0, T; \mathbf{H}^r(\Omega_c))} \right). \end{aligned}$$

Furthermore, assume that $(\vec{\mathbf{u}}, p) = (p_m, p_f, \mathbf{u}_c, p) \in H^1(0, T; H_{\Gamma_d}^{r+1} \times H_{\Gamma_d}^{r+1} \times \mathbf{H}_{\Gamma_c}^{r+1}) \times H^1(0, T; \mathbf{H}^r(\Omega_c))$; then we have

$$(4.26) \quad \begin{aligned} & \|\partial_t \vec{\mathbf{u}} - \partial_t \mathbb{P}_s \vec{\mathbf{u}}\|_{L^2(0, T; H_{\Gamma_d}^1 \times H_{\Gamma_d}^1 \times \mathbf{H}_{\Gamma_c}^1)} + \|\partial_t p - \partial_t \mathbb{P}_p p\|_{L^2(0, T; M)} \\ & \leq Ch^r \left(\|\vec{\mathbf{u}}\|_{H^1(0, T; H_{\Gamma_d}^{r+1} \times H_{\Gamma_d}^{r+1} \times \mathbf{H}_{\Gamma_c}^{r+1})} + \|p\|_{H^1(0, T; \mathbf{H}^r(\Omega_c))} \right). \end{aligned}$$

Proof. The proof of (4.25) follows the same argument as in Proposition 4.1 of [22]. Hence we only prove the inequality (4.26) here. Differentiating (4.23)–(4.24) with respect to t , we obtain

$$(4.27) \quad \begin{aligned} & a_\eta(\partial_t \vec{\mathbf{u}} - \partial_t \mathbb{P}_s \vec{\mathbf{u}}, \vec{\mathbf{v}}_h) + C_{0,\eta} \langle \partial_t \vec{\mathbf{u}} - \partial_t \mathbb{P}_s \vec{\mathbf{u}}, \vec{\mathbf{v}}_h \rangle_\eta \\ & \quad + b_\eta(\partial_t p - \partial_t \mathbb{P}_p p, \mathbf{v}_h) = 0, \end{aligned}$$

$$(4.28) \quad b_\eta(q_h, \partial_t \mathbf{u}_c - \partial_t \mathbb{P}_{s3} \mathbf{u}_c) = 0$$

for any $\vec{\mathbf{v}}_h = (\psi_{mh}, \psi_{fh}, \mathbf{v}_h) \in \mathbf{X}_0^h$ and $q_h \in M^h$. Define $\vec{\mathbf{e}}_h = \partial_t \vec{\mathbf{u}} - \partial_t \mathbb{P}_s \vec{\mathbf{u}}$. Based on $\vec{\mathbf{v}}_h - \partial_t \mathbb{P}_s \vec{\mathbf{u}} \in \mathbf{X}_0^h$, the definition of projection operator Π^h in (4.4), and (4.28), (4.27) leads to

$$(4.29) \quad \begin{aligned} & a_\eta(\vec{\mathbf{e}}_h, \vec{\mathbf{e}}_h) + C_{0,\eta} \langle \vec{\mathbf{e}}_h, \vec{\mathbf{e}}_h \rangle_\eta \\ & = a_\eta(\vec{\mathbf{e}}_h, \partial_t \vec{\mathbf{u}} - \vec{\mathbf{v}}_h) + C_{0,\eta} \langle \vec{\mathbf{e}}_h, \partial_t \vec{\mathbf{u}} - \vec{\mathbf{v}}_h \rangle_\eta - b_\eta(\partial_t p - \partial_t \mathbb{P}_p p, \mathbf{v}_h - \partial_t \mathbb{P}_{s3} \mathbf{u}_c) \\ & = a_\eta(\vec{\mathbf{e}}_h, \partial_t \vec{\mathbf{u}} - \vec{\mathbf{v}}_h) + C_{0,\eta} \langle \vec{\mathbf{e}}_h, \partial_t \vec{\mathbf{u}} - \vec{\mathbf{v}}_h \rangle_\eta - b_\eta(\partial_t p - \partial_t \mathbb{P}_p p, \mathbf{v}_h - \partial_t \Pi^h \mathbf{u}_c) \\ & \quad - b_\eta(\partial_t p - \partial_t q_h, \partial_t \Pi^h \mathbf{u}_c - \partial_t \mathbf{u}_c) \\ & = a_\eta(\vec{\mathbf{e}}_h, \partial_t \vec{\mathbf{u}} - \vec{\mathbf{v}}_h) + C_{0,\eta} \langle \vec{\mathbf{e}}_h, \partial_t \vec{\mathbf{u}} - \vec{\mathbf{v}}_h \rangle_\eta - b_\eta(\partial_t p - \partial_t q_h, \partial_t \Pi^h \mathbf{u}_c - \partial_t \mathbf{u}_c). \end{aligned}$$

Now let $\mathbf{v}_h = \partial_t \Pi^h \mathbf{u}_c$ and $\vec{\mathbf{v}}_h = (\psi_{mh}, \psi_{fh}, \partial_t \Pi^h \mathbf{u}_c)$ in (4.29). Together with the Gårding-type inequality (3.16), the Cauchy–Schwarz inequality, and Young’s inequality, we obtain the following estimate:

$$\begin{aligned} & C_{1,\eta} \|\vec{\mathbf{e}}_h\|_1^2 - C_{0,\eta} \|\vec{\mathbf{e}}_h\|_0^2 + C_{0,\eta} \|\vec{\mathbf{e}}_h\|_0^2 \\ & \leq a_\eta(\vec{\mathbf{e}}_h, \vec{\mathbf{e}}_h) + C_{0,\eta} \langle \vec{\mathbf{e}}_h, \vec{\mathbf{e}}_h \rangle_\eta \\ & = a_\eta(\vec{\mathbf{e}}_h, \partial_t \vec{\mathbf{u}} - \vec{\mathbf{v}}_h) + C_{0,\eta} \langle \vec{\mathbf{e}}_h, \partial_t \vec{\mathbf{u}} - \vec{\mathbf{v}}_h \rangle_\eta \\ & \quad - b_\eta(\partial_t p - \partial_t q_h, \partial_t \Pi^h \mathbf{u}_c - \partial_t \mathbf{u}_c) - b_\eta(\partial_t p - \partial_t q_h, \partial_t \mathbf{u}_c - \partial_t \mathbb{P}_{s3} \mathbf{u}_c) \\ & \leq C(\|\vec{\mathbf{e}}_h\|_1 \|\partial_t \vec{\mathbf{u}} - \vec{\mathbf{v}}_h\|_1 + \|\partial_t p - \partial_t q_h\|_0 \|\partial_t \Pi^h \mathbf{u}_c - \partial_t \mathbf{u}_c\|_1 + \|\partial_t p - \partial_t q_h\|_0 \|\vec{\mathbf{e}}_h\|_1) \\ & \leq \frac{C_{1,\eta}}{2} \|\vec{\mathbf{e}}_h\|_1^2 + C(\|\partial_t \vec{\mathbf{u}} - \vec{\mathbf{v}}_h\|_1^2 + \|\partial_t p - \partial_t q_h\|_0^2 + \|\partial_t \Pi^h \mathbf{u}_c - \partial_t \mathbf{u}_c\|_1^2), \end{aligned}$$

which implies that

$$(4.30) \quad \|\vec{\mathbf{e}}_h\|_1 \leq C(\|\partial_t \vec{\mathbf{u}} - \vec{\mathbf{v}}_h\|_1 + \|\partial_t p - \partial_t q_h\|_0 + \|\partial_t \Pi^h \mathbf{u}_c - \partial_t \mathbf{u}_c\|_1).$$

By the same argument with the div-stability condition in Proposition 4.1 of [22], we have

$$(4.31) \quad \|\partial_t p - \partial_t \mathbb{P}_p p\|_0 \leq C(\|\partial_t \vec{\mathbf{u}} - \vec{\mathbf{v}}_h\|_1 + \|\partial_t p - \partial_t q_h\|_0 + \|\partial_t \Pi^h \mathbf{u}_c - \partial_t \mathbf{u}_c\|_1).$$

Combining (4.30), (4.31), (4.2), (4.3), and (4.5), we complete the proof of (4.26). \square

Furthermore, we assume

$$(4.32) \quad a_\eta(\vec{\mathbf{u}}, \vec{\mathbf{v}}) + C_{0,\eta} \langle \vec{\mathbf{u}}, \vec{\mathbf{v}} \rangle_\eta + b_\eta(p, \mathbf{v}) = \ell_\eta(\vec{\mathbf{v}}) \quad \forall \vec{\mathbf{v}} = (\psi_m, \psi_f, \mathbf{v}) \in \mathbf{X}_0,$$

$$(4.33) \quad b_\eta(q, \mathbf{u}_c) = 0 \quad \forall q \in M$$

is regular in the sense of

$$(4.34) \quad \|\vec{\mathbf{u}}\|_2 + \|p\|_1 \leq C\|\ell_\eta\|_0,$$

where the solution $\vec{\mathbf{u}} = (p_m, p_f, \mathbf{u}_c) \in X_0$. Then we have the following Aubin–Nitsche-type estimate on $\|\vec{\mathbf{u}} - \mathbb{P}_s \vec{\mathbf{u}}\|_{\mathbf{L}^2}$.

LEMMA 5. *Under the assumptions of Lemma 4, we have the estimates*

$$(4.35) \quad \begin{aligned} & \|\vec{\mathbf{u}} - \mathbb{P}_s \vec{\mathbf{u}}\|_{L^q(0,T;\mathbf{L}^2)} + h\|p - \mathbb{P}_p p\|_{L^q(0,T;M)} \\ & \leq Ch^{r+1} \left(\|\vec{\mathbf{u}}\|_{L^q(0,T;H_{\Gamma_d}^{r+1} \times H_{\Gamma_d}^{r+1} \times \mathbf{H}_{\Gamma_c}^{r+1})} + \|p\|_{L^q(0,T;\mathbf{H}^r(\Omega_c))} \right), \end{aligned}$$

$$(4.36) \quad \begin{aligned} & \|\partial_t \vec{\mathbf{u}} - \partial_t \mathbb{P}_s \vec{\mathbf{u}}\|_{L^2(0,T;\mathbf{L}^2)} + h\|\partial_t p - \partial_t \mathbb{P}_p p\|_{L^2(0,T;M)} \\ & \leq Ch^{r+1} \left(\|\vec{\mathbf{u}}\|_{H^1(0,T;H_{\Gamma_d}^{r+1} \times H_{\Gamma_d}^{r+1} \times \mathbf{H}_{\Gamma_c}^{r+1})} + \|p\|_{H^1(0,T;\mathbf{H}^r(\Omega_c))} \right). \end{aligned}$$

Proof. The proof of (4.35) follows the same argument as in Proposition 4.3 of [22]. Hence we only prove (4.36) here. Define $\vec{\mathbf{e}}_h = \partial_t \vec{\mathbf{u}} - \partial_t \mathbb{P}_s \vec{\mathbf{u}} = (\partial_t p_m, \partial_t p_f, \partial_t \mathbf{u}_c) - (\partial_t \mathbb{P}_{s1} p_m, \partial_t \mathbb{P}_{s2} p_f, \partial_t \mathbb{P}_{s3} \mathbf{u}_c)$. Consider

$$(4.37) \quad a_\eta(\vec{\mathbf{u}}^d, \vec{\mathbf{v}}) + C_{0,\eta} \langle \vec{\mathbf{u}}^d, \vec{\mathbf{v}} \rangle_\eta + b_\eta(p^d, \mathbf{v}) = \langle \vec{\mathbf{e}}_h, \vec{\mathbf{v}} \rangle_\eta$$

$$\forall \vec{\mathbf{v}} = (\psi_m, \psi_f, \mathbf{v}) \in \mathbf{X}_0,$$

$$(4.38) \quad b_\eta(q, \mathbf{u}_c^d) = 0 \quad \forall q \in M.$$

Then (4.34) leads to

$$(4.39) \quad \|\vec{\mathbf{u}}^d\|_2 + \|p^d\|_1 \leq C\|\vec{\mathbf{e}}_h\|_0.$$

Choose $\vec{\mathbf{v}} = \vec{\mathbf{e}}_h$ and $\mathbf{v} = \partial_t \mathbf{u}_c - \partial_t \mathbb{P}_{s3} \mathbf{u}_c$ in (4.37). Then, by using (4.27), (4.28), (4.38), and the Cauchy–Schwarz inequality, for any $\vec{\mathbf{v}}_h \in X_0^h$ and $q_h \in M^h$, we obtain

$$(4.40) \quad \begin{aligned} & C\|\vec{\mathbf{e}}_h\|_0^2 \\ & \leq \langle \vec{\mathbf{e}}_h, \vec{\mathbf{e}}_h \rangle_\eta \\ & = a_\eta(\vec{\mathbf{u}}^d - \vec{\mathbf{v}}_h, \vec{\mathbf{e}}_h) + C_{0,\eta} \langle \vec{\mathbf{u}}^d - \vec{\mathbf{v}}_h, \vec{\mathbf{e}}_h \rangle_\eta + b_\eta(p^d - q_h, \partial_t \mathbf{u}_c - \partial_t \mathbb{P}_{s3} \mathbf{u}_c) \\ & \quad + a_\eta(\vec{\mathbf{v}}_h, \vec{\mathbf{e}}_h) + C_{0,\eta} \langle \vec{\mathbf{v}}_h, \vec{\mathbf{e}}_h \rangle_\eta + b_\eta(q_h, \partial_t \mathbf{u}_c - \partial_t \mathbb{P}_{s3} \mathbf{u}_c) \\ & = a_\eta(\vec{\mathbf{u}}^d - \vec{\mathbf{v}}_h, \vec{\mathbf{e}}_h) + C_{0,\eta} \langle \vec{\mathbf{u}}^d - \vec{\mathbf{v}}_h, \vec{\mathbf{e}}_h \rangle_\eta + b_\eta(p^d - q_h, \partial_t \mathbf{u}_c - \partial_t \mathbb{P}_{s3} \mathbf{u}_c) \\ & \quad + b_\eta(\partial_t p - \partial_t \mathbb{P}_p p, \mathbf{u}_c^d - \mathbf{v}_h) \end{aligned}$$

$$\leq C(\|\vec{\mathbf{e}}_h\|_1 + \|\partial_t p - \partial_t \mathbb{P}_p p\|_0) \times \left(\inf_{\vec{\mathbf{v}}_h \in \mathbf{X}_0^h} \|\vec{\mathbf{u}}^d - \vec{\mathbf{v}}_h\|_1 + \inf_{q_h \in M^h} \|p^d - q_h\|_0 \right),$$

where C is a generic constant whose value may be different from line to line. Using (4.2), (4.3), and (4.39), we get

$$(4.41) \quad \inf_{\vec{\mathbf{v}}_h \in \mathbf{X}_0^h} \|\vec{\mathbf{u}}^d - \vec{\mathbf{v}}_h\|_1 + \inf_{q_h \in M^h} \|p^d - q_h\|_0 \leq Ch(\|\vec{\mathbf{u}}^d\|_2 + \|p^d\|_1) \leq Ch\|\vec{\mathbf{e}}_h\|_0.$$

Plugging (4.41) into (4.40), integrating (4.40) with respect to t , and applying (4.26), we obtain

$$(4.42) \quad \|\vec{\mathbf{e}}_h\|_{L^2(0,T;\mathbf{L}^2)} \leq Ch^{r+1}(\|\vec{\mathbf{u}}\|_{H^1(0,T;H_{\Gamma_d}^{r+1} \times H_{\Gamma_d}^{r+1} \times \mathbf{H}_{\Gamma_c}^{r+1})} + \|p\|_{H^1(0,T;\mathbf{H}^r(\Omega_c))}).$$

Combining (4.42) and (4.26), the proof of (4.36) is completed. □

Define

$$\|\vec{\mathbf{u}}\|_{0,\eta} := \left(\|p_m\|_{H_{\Gamma_d}^1}^2 + \|p_f\|_{H_{\Gamma_d}^1}^2 + \|\eta^{\frac{1}{2}} \mathbf{u}_c\|_{\mathbf{H}_{\Gamma_c}^1}^2 \right)^{1/2}$$

for any $\vec{\mathbf{u}} = (p_m, p_f, \mathbf{u}_c) \in X_0$. Finally, we follow the standard energy method framework [22, 38, 83, 89] to analyze the full discretization error $\vec{\mathbf{u}}(t_n) - \vec{\mathbf{u}}_h^n$.

THEOREM 6. *Assume that $0 < r \leq k$, the solution $(\vec{\mathbf{u}}, p)$ of the system (3.11)–(3.12) satisfies $\partial_{tt} \vec{\mathbf{u}} \in L^2(0, T; \mathbf{L}^2)$, $(\vec{\mathbf{u}}, p) \in H^1(0, T; H_{\Gamma_d}^{r+1} \times H_{\Gamma_d}^{r+1} \times \mathbf{H}_{\Gamma_c}^{r+1}) \times H^1(0, T; \mathbf{H}^r(\Omega_c))$, $(\vec{\mathbf{u}}, p) \in L^\infty(0, T; H_{\Gamma_d}^{r+1} \times H_{\Gamma_d}^{r+1} \times \mathbf{H}_{\Gamma_c}^{r+1}) \times L^\infty(0, T; \mathbf{H}^r(\Omega_c))$, and the regularity property (4.34) of problem (4.32)–(4.33) holds. Let $(\vec{\mathbf{u}}_h^n, p_h^n)$ be the solution of the backward Euler scheme (4.17), and assume that the initial approximation $\vec{\mathbf{u}}_h^0$ of $\vec{\mathbf{u}}(0)$ satisfies $\|\vec{\mathbf{u}}_h^0 - \mathbb{P}_s \vec{\mathbf{u}}(0)\|_{\mathbf{L}^2} \leq C^* h^{r+1}$. Then we have the following estimate:*

$$(4.43) \quad \|\vec{\mathbf{u}}(t_n) - \vec{\mathbf{u}}_h^n\|_{0,\eta} \leq C \left[h^{r+1} + \Delta t \|\partial_{tt} \vec{\mathbf{u}}\|_{L^2(0,T;\mathbf{L}^2)} + h^{r+1} (\|\vec{\mathbf{u}}\|_{H^1(0,T;H_{\Gamma_d}^{r+1} \times H_{\Gamma_d}^{r+1} \times \mathbf{H}_{\Gamma_c}^{r+1})} + \|p\|_{H^1(0,T;\mathbf{H}^r(\Omega_c))} + \|\vec{\mathbf{u}}\|_{L^\infty(0,T;H_{\Gamma_d}^{r+1} \times H_{\Gamma_d}^{r+1} \times \mathbf{H}_{\Gamma_c}^{r+1})} + \|p\|_{L^\infty(0,T;\mathbf{H}^r(\Omega_c))}) \right].$$

Proof. Taking $\vec{\mathbf{v}} = \vec{\mathbf{v}}_h = (\psi_{mh}, \psi_{fh}, \mathbf{v}_h)$ in (3.11) and $q = q_h$ in (3.12) and subtracting (4.17)–(4.18) from (3.11)–(3.12) with $t = t_n$, we get

$$(4.44) \quad \left\langle \partial_t \vec{\mathbf{u}}(t_n) - \frac{\vec{\mathbf{u}}_h^n - \vec{\mathbf{u}}_h^{n-1}}{\Delta t}, \vec{\mathbf{v}}_h \right\rangle_\eta + a_\eta(\vec{\mathbf{u}}(t_n) - \vec{\mathbf{u}}_h^n, \vec{\mathbf{v}}_h)$$

$$(4.45) \quad + b_\eta(p(t_n) - p_h^n, \mathbf{v}_h) = 0,$$

$$b_\eta(q_h, \mathbf{u}_c(t_n) - \mathbf{u}_{ch}^n) = 0.$$

Define

$$(4.46) \quad \begin{aligned} \vec{\theta}^n &= \mathbb{P}_s \vec{\mathbf{u}}(t_n) - \vec{\mathbf{u}}_h^n, \quad \vec{\rho}^n = \vec{\mathbf{u}}(t_n) - \mathbb{P}_s \vec{\mathbf{u}}(t_n), \\ \theta^n &= \mathbb{P}_p p(t_n) - p_h^n, \quad \rho^n = p(t_n) - \mathbb{P}_p p(t_n), \end{aligned}$$

where

$$\begin{aligned} \vec{\theta}^n &= (\theta_m^n, \theta_f^n, \theta_c^n), \quad \theta_m^n = \mathbb{P}_{s1} p_m(t_n) - p_{mh}^n, \\ \theta_f^n &= \mathbb{P}_{s2} p_f(t_n) - p_{fh}^n, \quad \theta_c^n = \mathbb{P}_{s3} \mathbf{u}_c(t_n) - \mathbf{u}_{ch}^n, \\ \vec{\rho}^n &= (\rho_m^n, \rho_f^n, \rho_c^n), \quad \rho_m^n = p_m(t_n) - \mathbb{P}_{s1} p_m(t_n), \\ \rho_f^n &= p_f(t_n) - \mathbb{P}_{s2} p_f(t_n), \quad \rho_c^n = \mathbf{u}_c(t_n) - \mathbb{P}_{s3} \mathbf{u}_c(t_n). \end{aligned}$$

Then

$$(4.47) \quad \partial_t \vec{\mathbf{u}}(t_n) - \frac{\vec{\mathbf{u}}_h^n - \vec{\mathbf{u}}_h^{n-1}}{\Delta t} = \vec{\omega}_1^n + \vec{\omega}_2^n + \frac{\vec{\theta}^n - \vec{\theta}^{n-1}}{\Delta t},$$

where

$$\vec{\omega}_1^n = \partial_t \vec{\mathbf{u}}(t_n) - \frac{\vec{\mathbf{u}}(t_n) - \vec{\mathbf{u}}(t_{n-1})}{\Delta t}, \quad \vec{\omega}_2^n = \frac{\vec{\mathbf{u}}(t_n) - \vec{\mathbf{u}}(t_{n-1})}{\Delta t} - \mathbb{P}_s \left(\frac{\vec{\mathbf{u}}(t_n) - \vec{\mathbf{u}}(t_{n-1})}{\Delta t} \right).$$

Taking $\vec{\mathbf{v}}_h = \vec{\theta}^n$ and $q_h = \theta^n$ in (4.23)–(4.24) and (4.44)–(4.45), and using (4.46)–(4.47), we get

$$(4.48) \quad \left\langle \vec{\omega}_1^n + \vec{\omega}_2^n + \frac{\vec{\theta}^n - \vec{\theta}^{n-1}}{\Delta t}, \vec{\theta}^n \right\rangle_{\eta} + a_{\eta}(\vec{\theta}^n, \vec{\theta}^n)$$

$$(4.49) \quad \begin{aligned} &+ b_{\eta}(\theta^n, \theta_c^n) - C_{0,\eta} \langle \vec{\rho}^n, \vec{\theta}^n \rangle_{\eta} = 0, \\ b_{\eta}(\theta^n, \theta_c^n) &= 0. \end{aligned}$$

Hence we have

$$(4.50) \quad \begin{aligned} &\left\langle \frac{\vec{\theta}^n - \vec{\theta}^{n-1}}{\Delta t}, \vec{\theta}^n \right\rangle_{\eta} + a_{\eta}(\vec{\theta}^n, \vec{\theta}^n) \\ &= -\langle \vec{\omega}_1^n, \vec{\theta}^n \rangle_{\eta} - \langle \vec{\omega}_2^n, \vec{\theta}^n \rangle_{\eta} + C_{0,\eta} \langle \vec{\rho}^n, \vec{\theta}^n \rangle_{\eta}. \end{aligned}$$

Applying $(a - b)a = \frac{a^2 - b^2}{2} + \frac{(a-b)^2}{2}$ to the first term of (4.50) and summing (4.50) over $n = 1, \dots, m$, we get

$$(4.51) \quad \begin{aligned} &\|\vec{\theta}^m\|_{0,\eta}^2 + \sum_{n=1}^m (\Delta t)^2 \left\| \frac{\vec{\theta}^n - \vec{\theta}^{n-1}}{\Delta t} \right\|_{0,\eta}^2 + 2 \sum_{n=1}^m \Delta t a_{\eta}(\vec{\theta}^n, \vec{\theta}^n) \\ &= \|\vec{\theta}^0\|_{0,\eta}^2 - 2 \sum_{n=1}^m \Delta t \langle \vec{\omega}_1^n, \vec{\theta}^n \rangle_{\eta} - 2 \sum_{n=1}^m \Delta t \langle \vec{\omega}_2^n, \vec{\theta}^n \rangle_{\eta} \\ &+ 2 \sum_{n=1}^m C_{0,\eta} \Delta t \langle \vec{\rho}^n, \vec{\theta}^n \rangle_{\eta}. \end{aligned}$$

Based on Taylor’s expansion and Lemma 5, we recall the same arguments of Theorem 4.4 in [22] to analyze the last three terms on the right-hand side in (4.51). Then we obtain

$$\begin{aligned}
 & \|\vec{\theta}^m\|_{0,\eta}^2 + \sum_{n=1}^m (\Delta t)^2 \left\| \frac{\vec{\theta}^n - \vec{\theta}^{n-1}}{\Delta t} \right\|_{0,\eta}^2 \\
 & + 2 \sum_{n=1}^m \Delta t a_\eta(\vec{\theta}^n, \vec{\theta}^n) + 2 \sum_{n=1}^m \Delta t C_{0,\eta} \langle \vec{\theta}^n, \vec{\theta}^n \rangle_\eta \\
 \leq & \|\vec{\theta}^0\|_{0,\eta}^2 + 6\eta(\Delta t)^2 \|\partial_{tt} \vec{u}\|_{L^2(0,T;\mathbf{L}^2)}^2 + \frac{1}{2} \sum_{n=1}^m \Delta t \|\vec{\theta}^n\|_{0,\eta}^2 + 2 \sum_{n=1}^m \Delta t C_{0,\eta} \|\vec{\theta}^n\|_{0,\eta}^2 \\
 & + Ch^{2(r+1)} \left(\|\vec{u}\|_{H^1(0,T;H_{\Gamma_d}^{r+1} \times H_{\Gamma_d}^{r+1} \times \mathbf{H}_{\Gamma_c}^{r+1})}^2 + \|p\|_{H^1(0,T;\mathbf{H}^r(\Omega_c))}^2 \right) \\
 (4.52) \quad & + \|\vec{u}\|_{L^\infty(0,T;H_{\Gamma_d}^{r+1} \times H_{\Gamma_d}^{r+1} \times \mathbf{H}_{\Gamma_c}^{r+1})}^2 + \|p\|_{L^\infty(0,T;\mathbf{H}^r(\Omega_c))}^2.
 \end{aligned}$$

By using Gronwall’s inequality, we obtain

$$\begin{aligned}
 & \|\vec{\theta}^m\|_{0,\eta}^2 + \sum_{n=1}^m (\Delta t)^2 \left\| \frac{\vec{\theta}^n - \vec{\theta}^{n-1}}{\Delta t} \right\|_{0,\eta}^2 \\
 & + 2 \sum_{n=1}^m \Delta t a_\eta(\vec{\theta}^n, \vec{\theta}^n) + 2 \sum_{n=1}^m \Delta t C_{0,\eta} \langle \vec{\theta}^n, \vec{\theta}^n \rangle_\eta \\
 \leq & C \left[\|\vec{\theta}^0\|_{0,\eta}^2 + \Delta t^2 \|\partial_{tt} \vec{u}\|_{L^2(0,T;\mathbf{L}^2)}^2 \right. \\
 & + h^{2(r+1)} \left(\|\vec{u}\|_{H^1(0,T;H_{\Gamma_d}^{r+1} \times H_{\Gamma_d}^{r+1} \times \mathbf{H}_{\Gamma_c}^{r+1})}^2 + \|p\|_{H^1(0,T;\mathbf{H}^r(\Omega_c))}^2 \right) \\
 (4.53) \quad & \left. + \|\vec{u}\|_{L^\infty(0,T;H_{\Gamma_d}^{r+1} \times H_{\Gamma_d}^{r+1} \times \mathbf{H}_{\Gamma_c}^{r+1})}^2 + \|p\|_{L^\infty(0,T;\mathbf{H}^r(\Omega_c))}^2 \right].
 \end{aligned}$$

With the estimate for the initial approximation $\|\vec{\theta}^0\|_{0,\eta} \leq Ch^{r+1}$, we obtain

$$\begin{aligned}
 \|\vec{\theta}^m\|_{0,\eta}^2 \leq & C \left[h^{2(r+1)} + \Delta t \|\partial_{tt} \vec{u}\|_{L^2(0,T;\mathbf{L}^2)}^2 \right. \\
 & + h^{2(r+1)} \left(\|\vec{u}\|_{H^1(0,T;H_{\Gamma_d}^{r+1} \times H_{\Gamma_d}^{r+1} \times \mathbf{H}_{\Gamma_c}^{r+1})}^2 + \|p\|_{H^1(0,T;\mathbf{H}^r(\Omega_c))}^2 \right) \\
 (4.54) \quad & \left. + h^{2(r+1)} \left(\|\vec{u}\|_{L^\infty(0,T;H_{\Gamma_d}^{r+1} \times H_{\Gamma_d}^{r+1} \times \mathbf{H}_{\Gamma_c}^{r+1})}^2 + \|p\|_{L^\infty(0,T;\mathbf{H}^r(\Omega_c))}^2 \right) \right].
 \end{aligned}$$

Using (4.35), (4.54), and the triangle inequality

$$\|\vec{u}(t_n) - \vec{u}_h^n\|_{0,\eta} \leq \|\vec{u}(t_n) - \mathbb{P}_s \vec{u}(t_n)\|_{0,\eta} + \|\vec{\theta}^n\|_{0,\eta},$$

the proof of Theorem 6 can be completed. □

5. Numerical examples. In this section, we present four numerical examples to validate and illustrate the proposed model and finite element method. The quadratic finite elements and the Taylor–Hood finite elements [23] are used for the dual-porosity model and the Stokes equation, respectively. The Taylor–Hood finite elements satisfy the inf-sup condition (4.1). In the first example, we show the optimal convergence rates of the finite element method with the backward Euler scheme, the Crank–Nicolson scheme, and the two-step and three-step backward differentiation schemes for the time discretization. The second example simulates the flow around macrofractures. In the third example, we study the flow around a horizontal wellbore with open-hole completion. In the last example, we consider a multistage hydraulic fractured horizontal wellbore with cased hole completion.

5.1. Example 1. In the first example, which is to validate the proposed model and show the optimal convergence rates of the proposed finite element method, we consider the domain illustrated in Figure 1. The dual-porosity domain and the conduit domain are $\Omega_d = (0, 1) \times (0, 0.75)$ and $\Omega_c = (0, 1) \times (-0.25, 0)$, respectively. The interface between these two domains is $\Gamma_{cd} = (0, 1) \times \{0\}$. The parameters of the model are chosen as $\phi_m = 1$, $\phi_f = 1$, $k_m = 0.01$, $k_f = 1$, $\mu = 1$, $\nu = 1$, $\rho = 1$, $\sigma = 1$, $C_{mt} = 1$, $C_{ft} = 1$.

It is easy to verify that the following functions exactly satisfy the divergence-free equation (2.4) and the interface conditions (2.5)–(2.8):

$$(5.1) \quad p_m = \sin(xy^2 - y^3) \cos(t), \quad (x, y, t) \in \Omega_d \times [0, 1],$$

$$(5.2) \quad p_f = \left(2 - \pi \sin(\pi x)\right) \left(\cos(\pi(1 - y)) - y\right) \cos(2\pi t), \quad (x, y, t) \in \Omega_d \times [0, 1],$$

$$(5.3) \quad \mathbf{u}_c = \begin{pmatrix} \left(x^2 y^2 + \exp(-y)\right) \cos(2\pi t) \\ \left(-\frac{2}{3} x y^3 + (2 - \pi \sin(\pi x))\right) \cos(2\pi t) \end{pmatrix}, \quad (x, y, t) \in \Omega_c \times [0, 1],$$

$$(5.4) \quad p = \left(\pi \sin(\pi x) - 2\right) \cos(2\pi y) \cos(2\pi t), \quad (x, y, t) \in \Omega_c \times [0, 1].$$

Then the source terms, initial conditions, and Dirichlet boundary conditions of the model are chosen such that the above functions are the exact solutions of the model.

The numerical results at the time $T = 1$ with three different time step sizes $\Delta t = h$, h^2 , h^3 for the backward Euler scheme are listed in Tables 1–3. The numerical results at the time $T = 1$ with the time step size $\Delta t = h$ for the Crank–Nicolson scheme, the two-step backward differentiation scheme, and the three-step backward differentiation scheme are listed in Tables 4–6. The accuracy orders for the backward Euler scheme, the Crank–Nicolson scheme, the two-step backward differentiation scheme, and the three-step backward differentiation scheme in time are $O(\Delta t)$, $O(\Delta t^2)$, $O(\Delta t^2)$, and $O(\Delta t^3)$, respectively. Hence all the tables show the optimal convergence of the proposed finite element method in both the L^2 and H^1 norms with respect to the corresponding choices on Δt .

TABLE 1

The L^2 and H^1 errors and convergence orders for all variables at $T = 1$ with time step size $\Delta t = h$ for the backward Euler scheme.

L^2 error and convergence order								
h	$\ p_m - p_{mh}\ _0$	Rate	$\ p_f - p_{fh}\ _0$	Rate	$\ \mathbf{u}_c - \mathbf{u}_{ch}\ _0$	Rate	$\ p - p_h\ _0$	Rate
1/8	2.033e-3	0.89	4.058e-2	0.59	1.423e-2	0.49	2.119e-1	0.66
1/16	1.136e-3	0.84	2.526e-2	0.68	8.557e-3	0.73	1.228e-1	0.79
1/32	5.515e-4	1.04	1.313e-2	0.94	4.272e-3	1.00	6.019e-2	1.03
1/64	2.838e-4	0.96	6.967e-3	0.91	2.217e-3	0.95	3.097e-2	0.96
H^1 error and convergence order								
h	$\ p_m - p_{mh}\ _1$	Rate	$\ p_f - p_{fh}\ _1$	Rate	$\ \mathbf{u}_c - \mathbf{u}_{ch}\ _1$	Rate	$\ p - p_h\ _1$	Rate
1/8	2.125e-2	0.84	2.046e-1	0.92	1.308e-1	0.55	2.692e+00	0.73
1/16	1.188e-2	0.84	1.191e-1	0.78	7.854e-2	0.74	1.508e+00	0.84
1/32	5.756e-3	1.05	6.038e-2	0.98	3.930e-2	1.00	8.148e-1	0.89
1/64	2.959e-3	0.96	3.170e-2	0.93	2.043e-2	0.94	4.827e-1	0.76

TABLE 2

The L^2 and H^1 errors and convergence orders for all variables at $T = 1$ with time step size $\Delta t = h^2$ for the backward Euler scheme.

L^2 error and convergence order								
h	$\ p_m - p_{mh}\ _0$	Rate	$\ p_f - p_{fh}\ _0$	Rate	$\ \mathbf{u}_c - \mathbf{u}_{ch}\ _0$	Rate	$\ p - p_h\ _0$	Rate
1/8	3.968e-4	1.92	9.816e-3	1.84	3.076e-3	1.84	4.728e-2	1.91
1/16	1.002e-4	1.99	2.523e-3	1.96	7.830e-4	1.97	1.185e-2	2.00
1/32	2.510e-5	2.00	6.352e-4	1.99	1.967e-4	1.99	2.962e-3	2.00
1/64	6.278e-6	2.00	1.591e-4	2.00	4.927e-5	2.00	7.403e-4	2.00
H^1 error and convergence order								
h	$\ p_m - p_{mh}\ _1$	Rate	$\ p_f - p_{fh}\ _1$	Rate	$\ \mathbf{u}_c - \mathbf{u}_{ch}\ _1$	Rate	$\ p - p_h\ _1$	Rate
1/8	4.283e-3	1.87	8.332e-2	1.90	3.392e-2	1.83	1.425e+00	1.12
1/16	1.083e-3	1.98	2.124e-2	1.97	8.720e-3	1.96	6.518e-1	1.13
1/32	2.714e-4	2.00	5.341e-3	1.99	2.200e-3	1.99	3.165e-1	1.04
1/64	6.787e-5	2.00	1.338e-3	2.00	5.520e-4	1.99	1.570e-1	1.01

TABLE 3

The L^2 and H^1 errors and convergence orders for all variables at $T = 1$ with time step size $\Delta t = h^3$ for the backward Euler scheme.

L^2 error and convergence order								
h	$\ p_m - p_{mh}\ _0$	Rate	$\ p_f - p_{fh}\ _0$	Rate	$\ \mathbf{u}_c - \mathbf{u}_{ch}\ _0$	Rate	$\ p - p_h\ _0$	Rate
1/8	7.176e-5	2.92	2.169e-3	2.97	6.629e-4	2.91	2.036e-2	2.05
1/16	9.034e-6	2.99	2.665e-4	3.02	8.351e-5	2.99	4.710e-3	2.11
1/32	1.133e-6	3.00	3.292e-5	3.02	1.047e-5	3.00	1.143e-3	2.04
1/64	1.418e-7	3.00	4.090e-6	3.01	1.309e-6	3.00	2.833e-4	2.01
H^1 error and convergence order								
h	$\ p_m - p_{mh}\ _1$	Rate	$\ p_f - p_{fh}\ _1$	Rate	$\ \mathbf{u}_c - \mathbf{u}_{ch}\ _1$	Rate	$\ p - p_h\ _1$	Rate
1/8	1.373e-3	2.37	7.129e-2	1.96	2.045e-2	2.05	1.274e+00	0.87
1/16	3.047e-4	2.17	1.799e-2	1.99	5.027e-3	2.02	6.310e-1	1.01
1/32	7.352e-5	2.05	4.513e-3	1.99	1.253e-3	2.00	3.137e-1	1.01
1/64	1.821e-5	2.01	1.130e-3	2.00	3.134e-4	2.00	1.566e-1	1.00

5.2. Example 2. Research on fluid flow in fractures and fractured porous media has several decades of history [76]. The objective of this test is to investigate the flow characteristics around macrofractures, especially the effects of the macrofractures on the flow. Here we mainly focus on a conceptual geometric setup and the solution around the macrofractures to validate our model. We use the square $[0, 1.5]^2$ as the simulation domain, inside which there are macrofractures with different shapes; see Figure 2.

The parameters of the model are chosen as $\phi_m = 10^{-1}$, $\phi_f = 10^{-3}$, $k_m = 10^{-7}$, $k_f = 10^{-4}$, $\mu = 10^{-2}$, $\nu = 10^{-5}$, $\sigma = 10^{-1}$, $C_{mt} = 10^{-3}$, $C_{ft} = 10^{-3}$. As shown in Figures 2a and 2b, we impose a pressure drop from the boundary Γ_{in} to the boundary Γ_{out} and apply a homogeneous Neumann boundary condition on Γ_{no} :

$$p_m = 5 \times 10^3, p_f = 2 \times 10^3 \text{ on } \Gamma_{in}, p_m = 10^3, p_f = 10^3 \text{ on } \Gamma_{out},$$

$$-\frac{k_m}{\mu} \nabla p_m \cdot \mathbf{n} = 0, \quad -\frac{k_f}{\mu} \nabla p_f \cdot \mathbf{n} = 0 \text{ on } \Gamma_{no},$$

where \mathbf{n} is the outward unit normal to Γ_{no} . The proposed interface conditions (2.5)–

TABLE 4

The L^2 and H^1 errors and convergence orders for all variables at $T = 1$ with time step size $\Delta t = h$ for the Crank–Nicolson scheme.

L^2 error and convergence order								
h	$\ p_m - p_{mh}\ _0$	Rate	$\ p_f - p_{fh}\ _0$	Rate	$\ \mathbf{u}_c - \mathbf{u}_{ch}\ _0$	Rate	$\ p - p_h\ _0$	Rate
1/32	2.754e-6	2.15	2.773e-4	2.20	2.348e-5	2.27	2.406e-3	2.02
1/40	1.854e-6	1.77	1.861e-4	1.79	1.559e-5	1.83	1.395e-3	2.44
1/48	1.256e-6	2.13	1.258e-4	2.15	1.050e-5	2.17	9.691e-4	2.00
1/56	9.071e-7	2.11	9.073e-5	2.12	7.557e-6	2.14	7.122e-4	2.00
H^1 error and convergence order								
h	$\ p_m - p_{mh}\ _1$	Rate	$\ p_f - p_{fh}\ _1$	Rate	$\ \mathbf{u}_c - \mathbf{u}_{ch}\ _1$	Rate	$\ p - p_h\ _1$	Rate
1/32	7.954e-5	2.02	4.645e-3	2.01	1.301e-3	2.03	3.164e-1	1.04
1/40	5.138e-5	1.96	2.980e-3	1.99	8.308e-4	2.01	2.503e-1	1.05
1/48	3.553e-5	2.02	2.066e-3	2.01	5.761e-4	2.01	2.086e-1	1.00
1/56	2.603e-5	2.02	1.517e-3	2.01	4.229e-4	2.01	1.788e-1	1.00

TABLE 5

The L^2 and H^1 errors and convergence orders for all variables at $T = 1$ with time step size $\Delta t = h$ for the two-step backward differentiation method.

L^2 error and convergence order								
h	$\ p_m - p_{mh}\ _0$	Rate	$\ p_f - p_{fh}\ _0$	Rate	$\ \mathbf{u}_c - \mathbf{u}_{ch}\ _0$	Rate	$\ p - p_h\ _0$	Rate
1/32	1.049e-5	2.07	1.587e-3	2.46	2.404e-4	2.84	3.399e-3	2.78
1/40	7.130e-6	1.73	1.015e-3	2.00	1.439e-4	2.30	2.066e-3	2.23
1/48	4.866e-6	2.10	6.563e-4	2.39	8.746e-5	2.73	1.292e-3	2.57
1/56	3.531e-6	2.08	4.577e-4	2.34	5.805e-5	2.66	8.817e-4	2.48
H^1 error and convergence order								
h	$\ p_m - p_{mh}\ _1$	Rate	$\ p_f - p_{fh}\ _1$	Rate	$\ \mathbf{u}_c - \mathbf{u}_{ch}\ _1$	Rate	$\ p - p_h\ _1$	Rate
1/32	1.441e-4	2.04	7.675e-3	2.37	2.793e-3	2.64	3.199e-1	1.15
1/40	9.658e-5	1.79	4.892e-3	2.02	1.725e-3	2.16	2.542e-1	1.03
1/48	6.618e-5	2.07	3.238e-3	2.26	1.101e-3	2.47	2.108e-1	1.03
1/56	4.817e-5	2.06	2.301e-3	2.22	7.618e-4	2.39	1.802e-1	1.02

(2.8) are applied on Γ_{cd} .

The numerical results for the two cases at time $T = 1$ are shown in Figures 3 and 4, where the warmer color indicates higher speed of the flow and the line with arrows is the streamline. The mesh size is about $h \approx 0.0313$ for the first case and about $h \approx 0.0263$ for the second case. A constant time step size $\Delta t = 0.001$ is used. From the right plots in Figures 3 and 4, we can see that the flow in the matrix does not directly go into the macrofractures, which is consistent with the no-exchange interface condition (2.5). On the other hand, in the left plots of Figures 3 and 4, the flow in the microfractures interacts with the flow in the macrofractures based on the other three interface conditions (2.6)–(2.8). And the important effect of the tangential jump interface condition (2.8) can be easily observed. Moreover, the flow in the macrofractures is much faster than that of the dual-porosity media due to the high conductivity pathway provided by the macrofractures. It can also be observed in Figure 4 that the flow speed is higher as expected in the macrofracture which is along with the flow direction.

In the following, we will compare the results of the dual-porosity-Stokes model

TABLE 6

The L^2 and H^1 errors and convergence orders for all variables at $T = 1$ with time step size $\Delta t = h$ for the three-step backward differentiation method.

L^2 error and convergence order								
h	$\ p_m - p_{mh}\ _0$	Rate	$\ p_f - p_{fh}\ _0$	Rate	$\ \mathbf{u}_c - \mathbf{u}_{ch}\ _0$	Rate	$\ p - p_h\ _0$	Rate
1/32	6.842e-7	3.17	4.270e-4	2.47	1.487e-4	2.79	2.404e-3	2.73
1/40	3.737e-7	2.71	2.491e-4	2.42	8.472e-5	2.52	1.402e-3	2.42
1/48	2.086e-7	3.20	1.443e-4	2.99	4.822e-5	3.09	8.465e-4	2.77
1/56	1.280e-7	3.17	9.076e-5	3.01	2.996e-5	3.09	5.607e-4	2.67
H^1 error and convergence order								
h	$\ p_m - p_{mh}\ _1$	Rate	$\ p_f - p_{fh}\ _1$	Rate	$\ \mathbf{u}_c - \mathbf{u}_{ch}\ _1$	Rate	$\ p - p_h\ _1$	Rate
1/32	7.284e-5	2.02	4.938e-3	2.14	1.851e-3	2.52	3.139e-1	1.02
1/40	4.658e-5	2.00	3.114e-3	2.07	1.117e-3	2.26	2.509e-1	1.00
1/48	3.232e-5	2.00	2.115e-3	2.12	7.116e-4	2.47	2.089e-1	1.00
1/56	2.373e-5	2.00	1.533e-3	2.09	4.933e-4	2.38	1.790e-1	1.00

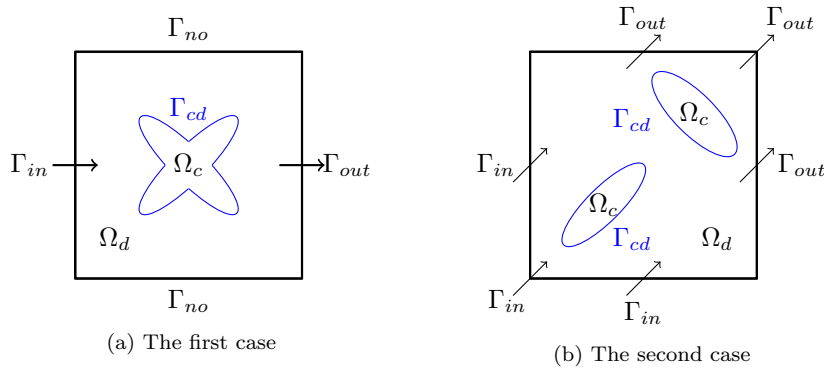


FIG. 2. An illustration of the domain, interface, and boundary for different shapes of macrofractures.

with the results of the corresponding Stokes–Darcy model. Since the Stokes–Darcy model only considers the matrix and macrofractures without the microfractures, we apply the same parameters of the matrix and macrofractures of the dual-porosity-Stokes model to the Darcy and Stokes parts of the Stokes–Darcy model. From the left plots of Figures 5 and 6, especially the value of the maximum speed, it is observed that the flow is much slower than that of the left plots of Figures 3 and 4 because the microfractures with much larger permeability are not considered in the Stokes–Darcy model. From the right plots of Figures 5 and 6, it is observed that the flow performance in the matrix is different from that of the right plots of Figures 3 and 4 due to the different communication properties between the matrix and the macrofractures. Therefore, the microfractures, which have much larger permeability than the matrix, should not be ignored for modeling a dual-porosity medium. For the dual-porosity media coupled with macrofractures or conduits, the newly proposed dual-porosity-Stokes model can provide more accurate and physically valid results since it accounts for the significant effect of the microfractures on the flow pathway.

5.3. Example 3. In this example, we simulate the flow around a horizontal production wellbore with open-hole completion [77]. As shown in Figure 7, a hor-

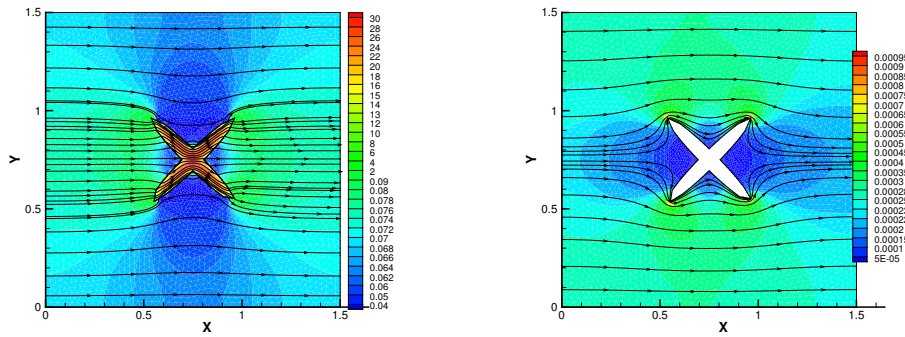


FIG. 3. Example 2: Flow speed and streamlines around two intersecting macrofractures for the dual-porosity-Stokes model. Left: the flow in microfractures and macrofractures; Right: the flow in the matrix.

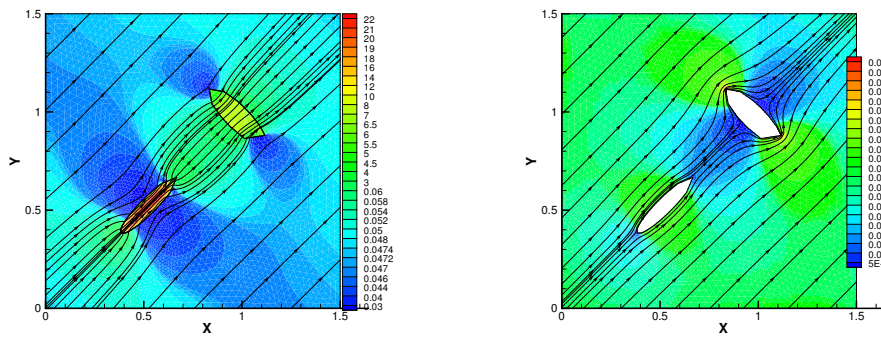


FIG. 4. Example 2: Flow speed and streamlines around two scattered macrofractures for the dual-porosity-Stokes model. Left: the flow in microfractures and macrofractures; Right: the flow in the matrix.

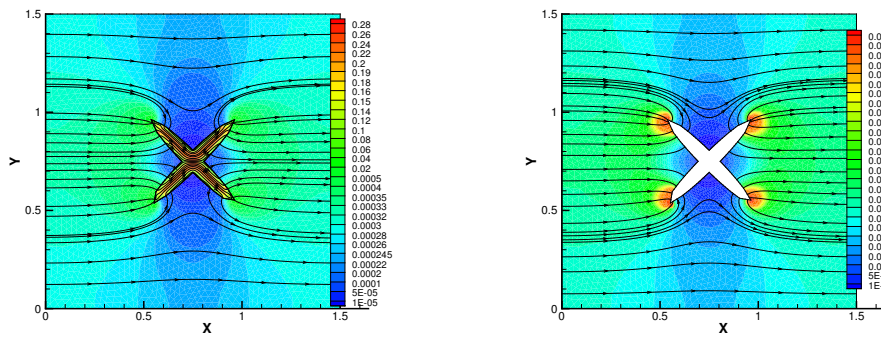


FIG. 5. Example 2: Flow speed and streamlines around two intersecting macrofractures for the Stokes-Darcy model. Left: the flow in the matrix and macrofractures; Right: the flow in the matrix only.

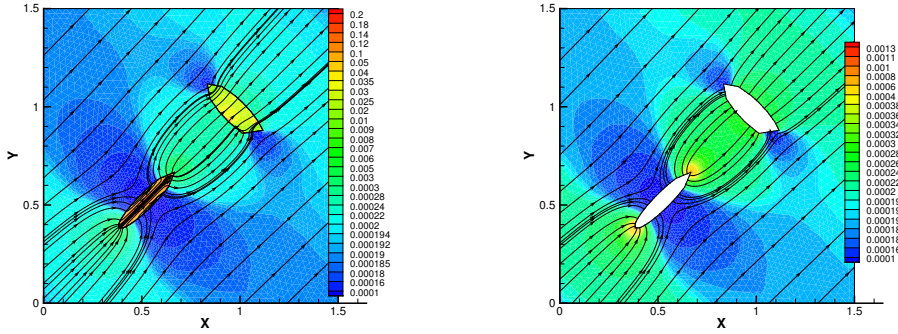


FIG. 6. Example 2: Flow speed and streamlines around two scattered macrofractures for the Stokes–Darcy model. Left: the flow in the matrix and macrofractures; Right: the flow in the matrix only.

horizontal cross-section is considered: the simulation domain is the square $[0, 2]^2$, and the horizontal wellbore is simplified as a rectangle $[0.6, 1.4] \times [0.9, 1.1]$ in this domain. With open-hole completion, the fluid in the microfractures can flow into the horizontal wellbore through the interface Γ_{cd} on which the proposed interface conditions (2.5)–(2.8) are applied. The vertical wellbore is connected to the horizontal wellbore at the boundary Γ_{out}^c on which the fluid in Ω_c does not communicate with Ω_d but directly flows out of the horizontal wellbore to the vertical wellbore. Therefore, the no-exchange boundary conditions $-\frac{k_f}{\mu} \nabla p_f \cdot (-\mathbf{n}_{cd}) = 0$ and $-\frac{k_m}{\mu} \nabla p_m \cdot (-\mathbf{n}_{cd}) = 0$ are imposed on Γ_{out}^c for the flow in the microfractures and matrix, respectively. The outflow boundary condition $\mathbb{T}(\mathbf{u}_c, p)\mathbf{n}_{cd} = 0$ is imposed on Γ_{out}^c for the free flow in Ω_c . Furthermore, we impose the constant pressure boundary condition for p_m and p_f on the domain boundary Γ_{in} : $p_m = 5 \times 10^4$, $p_f = 10^4$ on Γ_{in} . The parameters of the model are chosen as $\phi_m = 10^{-2}$, $\phi_f = 10^{-4}$, $k_m = 10^{-8}$, $k_f = 10^{-3}$, $\mu = 10^{-3}$, $\nu = 10^{-6}$, $\sigma = 0.9$, $C_{mt} = 10^{-4}$, $C_{ft} = 10^{-4}$.

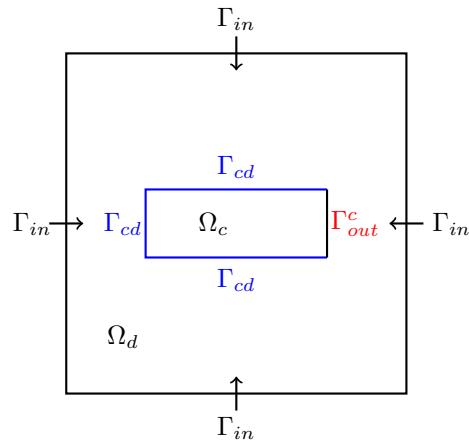


FIG. 7. An illustration of the domain, interface, and boundary for the horizontal wellbore with open-hole completion.

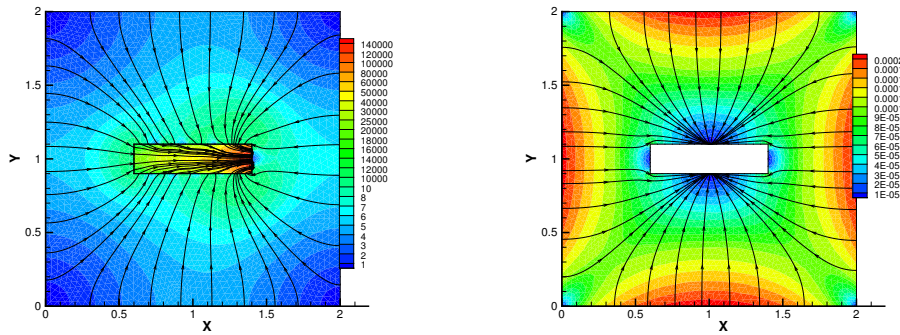


FIG. 8. Example 3: Flow speed and streamlines around a horizontal wellbore with open-hole completion and $\sigma = 0.9$. Left: the flow in microfractures and the horizontal wellbore; Right: the flow in the matrix.

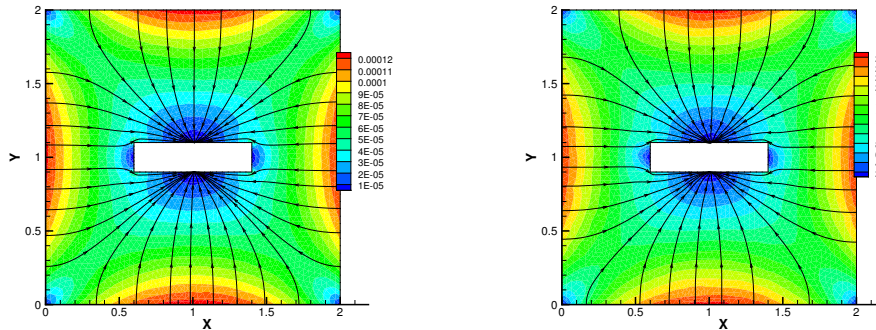


FIG. 9. Example 3: Flow speed and streamlines in the matrix. Left: $\sigma = 0.5$; Right: $\sigma = 0.1$.

The numerical results at the time $T = 2$ are shown in Figure 8. The mesh size is about $h \approx 0.0454$, and the time step size is $\Delta t = 0.002$. Based on the flow direction, we can see that the pressure near the wellbore is lower than elsewhere. The fluid flows from the matrix to the microfractures, then flows to the wellbore, and finally is produced with a faster speed from the right end of the horizontal wellbore where the vertical production wellbore is located. The physically valid results comply with the fundamental properties of the system consisting of dual-porosity media and conduits and hence illustrate the applicability of the proposed model and finite element method to the horizontal wellbore problem. In the next example, we will further extend our simulation to a more complicated realistic case.

Now we provide the results for different values of the shape factor σ , which ranges from 0 to 1. Based on Figures 8 and 9, we can see that larger σ can lead to a faster flow in the matrix. This is consistent with the effect of larger σ on increasing the production rate [1, 34].

5.4. Example 4. In this example, we simulate the flow around a multistage hydraulic fractured horizontal production wellbore with cased hole completion, which is important in the petroleum industry, especially for shale oil/gas production [13, 78,

81]. As shown in Figure 10, a horizontal cross-section is considered: the simulation domain is the square $[0, 6]^2$, and the horizontal wellbore is simplified as a rectangle $[1.8, 4.2] \times [2.8, 3.2]$ in this domain. With cased hole completion, the horizontal wellbore does not directly communicate with the dual-porosity media but is only fed by the hydraulic fractures [81]. Therefore, we imposed the following boundary conditions on Γ_{no}^c :

$$-\frac{k_f}{\mu} \nabla p_f \cdot (-\mathbf{n}_{cd}) = 0, \quad -\frac{k_m}{\mu} \nabla p_m \cdot (-\mathbf{n}_{cd}) = 0, \quad \mathbf{u}_c \cdot \mathbf{n}_{cd} = 0 \text{ on } \Gamma_{no}^c.$$

The fluid in the microfractures can flow into the hydraulic fractures through the interface Γ_{cd} on which the proposed interface conditions (2.5)–(2.8) are applied. The vertical wellbore is connected to the horizontal wellbore at the boundary Γ_{out}^c on which the fluid in Ω_c does not communicate with Ω_d but directly flows out of the horizontal wellbore to the vertical wellbore. Therefore, we imposed the following boundary conditions on Γ_{out}^c :

$$-\frac{k_f}{\mu} \nabla p_f \cdot (-\mathbf{n}_{cd}) = 0, \quad -\frac{k_m}{\mu} \nabla p_m \cdot (-\mathbf{n}_{cd}) = 0, \quad \mathbb{T}(\mathbf{u}_c, p) \mathbf{n}_{cd} = 0 \text{ on } \Gamma_{out}^c.$$

Furthermore, we impose the fixed pressure boundary condition for p_m and p_f on the domain boundary Γ_{in} : $p_m = 10^5$, $p_f = 10^4$ on Γ_{in} . The parameters of the model are chosen as $\phi_m = 10^{-2}$, $\phi_f = 10^{-5}$, $k_m = 10^{-9}$, $k_f = 10^{-3}$, $\mu = 10^{-3}$, $\nu = 10^{-6}$, $\sigma = 0.5$, $C_{mt} = 10^{-4}$, $C_{ft} = 10^{-4}$.

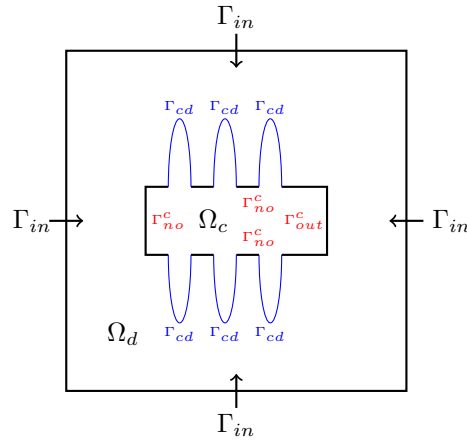


FIG. 10. A sample figure to explain the treatment of interface and boundary conditions for the multistage hydraulic fractured horizontal wellbore with cased hole completion.

The numerical results at the time $T = 4$ for smaller and larger hydraulic fractures are shown in Figures 11 and 12. The mesh size is about $h \approx 0.0332$ for the case with smaller fractures and about $h \approx 0.0456$ for the case of larger fractures. The time step size is $\Delta t = 0.004$. The flow goes from the matrix to the microfractures and then to the macrofractures only. In contrast with the results in the previous example, the fluid does not directly flow into the horizontal wellbore since the cased hole completion seals the interface between the horizontal wellbore and the dual-porosity media. As expected from the purpose of the hydraulic fractures, all the hydraulic fractures form attractions for the flow. The fluid is produced with a faster

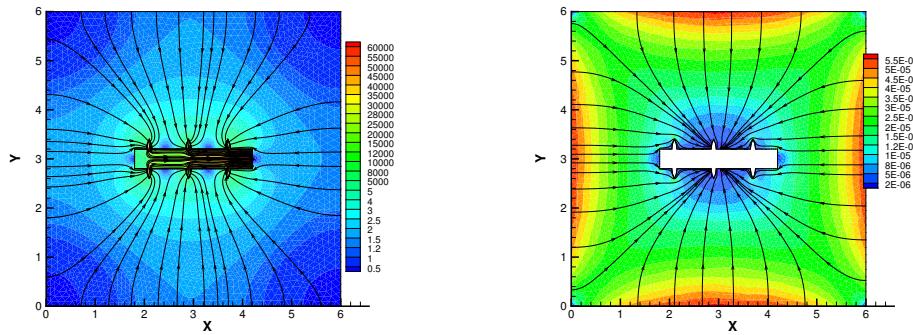


FIG. 11. *Example 4: Flow speed and streamlines around a multistage hydraulic fractured horizontal wellbore with cased hole completion. Left: the flow in microfractures and the multistage hydraulic fractured horizontal wellbore; Right: the flow in the matrix.*

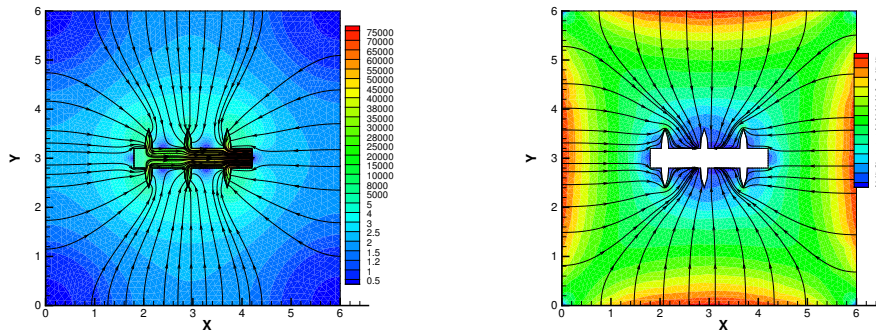


FIG. 12. *Example 4: Flow speed and streamlines around a multistage hydraulic fractured horizontal wellbore with cased hole completion and larger macrofractures. Left: the flow in microfractures and the multistage hydraulic fractured horizontal wellbore; Right: the flow in the matrix.*

speed from the right end of the horizontal wellbore where the vertical production wellbore is located. When we enlarge the size of the fractures, the productivity is dramatically increased due to the increase of the flow speed, as expected. These physically valid numerical results illustrate the complicated dynamic features of the dual-porosity-conduit interface system and hence further validate the feasibility of the proposed dual-porosity-Stokes model.

6. Conclusions. In this paper, a new dual-porosity-Stokes model is first proposed to govern the coupled flow in a dual-porosity media and the conduits/macrofractures which are embedded in or adjacent to the dual-porosity media. This model consists of a dual-porosity model in the dual-porosity media, the Stokes equation in the conduits and macrofractures, and four interface conditions to couple these two constituent models. Based on the fundamental properties of the chosen dual-porosity model and the traditional Stokes–Darcy problem, the four interface conditions include the no-exchange condition between the matrix and the conduits as well as the mass balance condition, the force balance condition, and the Beavers–Joseph condition. Compared with the traditional dual-porosity model which uses a source term to rep-

resent the effect of the wells, the Stokes equation and the interface conditions in the new model provide a more specific and accurate description for the flow in and around the conduits/macrofractures. The weak formulation of the new model is derived, and the well-posedness of the model is analyzed. A finite element method is proposed with four schemes in time discretization. The full discretization with the backward Euler scheme is analyzed. Four numerical experiments are presented. The optimal convergence order of the finite element method is clearly illustrated in the first experiment. The flow characteristics around macrofractures, the horizontal wellbore, and the multistage hydraulic fractured horizontal wellbore are investigated in the other three experiments. All of the numerical examples validate the proposed model and finite element method and illustrate their applicability to describe the complicated flow characteristics in the dual-porosity media coupled with conduits/macrofractures.

REFERENCES

- [1] A. S. A. ABUSHAIKHA AND O. R. GOSSELIN, *Matrix-fracture transfer function in dual-medium flow simulation-improved model of capillary imbibition*, in Proceedings of the 11th European Conference on the Mathematics of Oil Recovery, 2008.
- [2] R. AGUILERA, *Naturally Fractured Reservoirs*, Petroleum Publishing Company, Tulsa, OK, 1980.
- [3] T. ARBOGAST AND D. S. BRUNSON, *A computational method for approximating a Darcy-Stokes system governing a vuggy porous medium*, *Comput. Geosci.*, 11 (2007), pp. 207–218, doi:10.1007/s10596-007-9043-0.
- [4] T. ARBOGAST, J. DOUGLAS, JR., AND U. HORNING, *Derivation of the double porosity model of single phase flow via homogenization theory*, *SIAM J. Math. Anal.*, 21 (1990), pp. 823–836, doi:10.1137/0521046.
- [5] T. ARBOGAST AND M. GOMEZ, *A discretization and multigrid solver for a Darcy-Stokes system of three dimensional vuggy porous media*, *Comput. Geosci.*, 13 (2009), pp. 331–348, doi:10.1007/s10596-008-9121-y.
- [6] T. ARBOGAST AND H. L. LEHR, *Homogenization of a Darcy-Stokes system modeling vuggy porous media*, *Comput. Geosci.*, 10 (2006), pp. 291–302, doi:10.1007/s10596-006-9024-8.
- [7] I. BABUŠKA AND G. N. GATICA, *A residual-based a posteriori error estimator for the Stokes–Darcy coupled problem*, *SIAM J. Numer. Anal.*, 48 (2010), pp. 498–523, doi:10.1137/080727646.
- [8] L. BADEA, M. DISCACCIATI, AND A. QUARTERONI, *Numerical analysis of the Navier-Stokes/Darcy coupling*, *Numer. Math.*, 115 (2010), pp. 195–227, doi:10.1007/s00211-009-0279-6.
- [9] G. I. BARENBLATT, I. P. ZHELTOV, AND I. N. KOCHINA, *Basic concepts in the theory of seepage of homogeneous liquids in fissured rocks*, *J. Appl. Math. Mech.*, 24 (1960), pp. 1286–1303, doi:10.1016/0021-8928(60)90107-6.
- [10] G. BEAVERS AND D. JOSEPH, *Boundary conditions at a naturally permeable wall*, *J. Fluid Mech.*, 30 (1967), pp. 197–207, doi:10.1017/S0022112067001375.
- [11] R. O. BELLO AND R. A. WATTENBARGER, *Multi-stage hydraulically fractured horizontal shale gas well rate transient analysis*, SPE-126754, Society of Petroleum Engineers, North Africa Technical Conference and Exhibition, Cairo, Egypt, 2010.
- [12] R. O. BELLO AND R. A. WATTENBARGER, *Rate transient analysis in naturally fractured shale gas reservoirs*, SPE-114591, Society of Petroleum Engineers, CIPC/SPE Gas Technology Symposium 2008 Joint Conference, Calgary, Alberta, Canada, 2008.
- [13] R. O. BELLO AND R. A. WATTENBARGER, *Multi-stage hydraulically fractured shale gas rate transient analysis*, SPE-126754, Society of Petroleum Engineers, North Africa Technical Conference and Exhibition, Cairo, Egypt, 2010, pp. 14–17, doi:10.2118/126754-MS.
- [14] Y. BOUBENDIR AND S. TLUPOVA, *Domain decomposition methods for solving Stokes–Darcy problems with boundary integrals*, *SIAM J. Sci. Comput.*, 35 (2013), pp. B82–B106, doi:10.1137/110838376.
- [15] B. BOURBIAUX, S. GRANET, P. LANDEREAU, B. NOETINGER, S. SARDA, AND J. C. SABATHIER, *Scaling up matrix-fracture transfers in dual-porosity models: Theory and application*, SPE-56557, Society of Petroleum Engineers, SPE Annual Technical Conference and Exhibition, Houston, TX, 1999, doi:10.2118/56557-MS.

- [16] I. G. BROHI, M. POOLADI-DARVISH, AND R. AGUILERA, *Modeling fractured horizontal wells as dual porosity composite reservoirs - application to tight gas, shale gas and tight oil cases*, SPE-144057, Society of Petroleum Engineers, SPE Western North American Region Meeting, Anchorage, AK, 2011, doi:10.2118/144057-MS.
- [17] M. CAI, M. MU, AND J. XU, *Numerical solution to a mixed Navier–Stokes/Darcy model by the two-grid approach*, SIAM J. Numer. Anal., 47 (2009), pp. 3325–3338, doi:10.1137/080721868.
- [18] S. CAO, J. POLLASTRINI, AND Y. JIANG, *Separation and characterization of protein aggregates and particles by field flow fractionation*, Curr. Pharm. Biotechnol., 10 (2009), pp. 382–390, doi:10.2174/138920109788488978.
- [19] Y. CAO, Y. CHU, X.-M. HE, AND M. WEI, *Decoupling the stationary Navier–Stokes–Darcy system with the Beavers–Joseph–Saffman interface condition*, Abstr. Appl. Anal., 136483, 2013, doi:10.1155/2013/136483.
- [20] Y. CAO, M. GUNZBURGER, X.-M. HE, AND X. WANG, *Robin–Robin domain decomposition methods for the steady Stokes–Darcy model with Beaver–Joseph interface condition*, Numer. Math., 117 (2011), pp. 601–629, doi:10.1007/s00211-011-0361-8.
- [21] Y. CAO, M. GUNZBURGER, X.-M. HE, AND X. WANG, *Parallel, non-iterative, multi-physics domain decomposition methods for time-dependent Stokes–Darcy systems*, Math. Comp., 83 (2014), pp. 1617–1644, doi:10.1090/S0025-5718-2014-02779-8.
- [22] Y. CAO, M. GUNZBURGER, X. HU, F. HUA, X. WANG, AND W. ZHAO, *Finite element approximations for Stokes–Darcy flow with Beavers–Joseph interface conditions*, SIAM J. Numer. Anal., 47 (2010), pp. 4239–4256, doi:10.1137/080731542.
- [23] Y. CAO, M. GUNZBURGER, F. HUA, AND X. WANG, *Coupled Stokes–Darcy model with Beavers–Joseph interface boundary condition*, Commun. Math. Sci., 8 (2010), pp. 1–25, <http://citeseerx.ist.psu.edu/viewdoc/summary?doi=10.1.1.145.2746>.
- [24] E. S. CARLSON AND J. C. MERCER, *Devonian shale gas production: Mechanisms and simple models*, J. Petro. Technol., 43 (1991), pp. 476–482, doi:10.2118/19311-PA.
- [25] J. F. CARNEIRO, *Numerical simulations on the influence of matrix diffusion to carbon sequestration in double porosity fissured aquifers*, Int. J. Greenh. Gas Con., 3 (2009), pp. 431–443, doi:10.1016/j.ijggc.2009.02.006.
- [26] A. ÇEŞMELİOĞLU AND B. RIVIÈRE, *Analysis of time-dependent Navier–Stokes flow coupled with Darcy flow*, J. Numer. Math., 16 (2008), pp. 249–280, doi:10.1515/JNUM.2008.012.
- [27] A. ÇEŞMELİOĞLU AND B. RIVIÈRE, *Primal discontinuous Galerkin methods for time-dependent coupled surface and subsurface flow*, J. Sci. Comput., 40 (2009), pp. 115–140, doi:10.1007/s10915-009-9274-4.
- [28] J. CHEN, S. SUN, AND X. WANG, *A numerical method for a model of two-phase flow in a coupled free flow and porous media system*, J. Comput. Phys., 268 (2014), pp. 1–16, doi:10.1016/j.jcp.2014.02.043.
- [29] N. CHEN, M. GUNZBURGER, AND X. WANG, *Asymptotic analysis of the differences between the Stokes–Darcy system with different interface conditions and the Stokes–Brinkman system*, J. Math. Anal. Appl., 368 (2010), pp. 658–676, doi:10.1016/j.jmaa.2010.02.022.
- [30] W. CHEN, M. GUNZBURGER, F. HUA, AND X. WANG, *A parallel Robin–Robin domain decomposition method for the Stokes–Darcy system*, SIAM J. Numer. Anal., 49 (2011), pp. 1064–1084, doi:10.1137/080740556.
- [31] P. CHIDYAGWAI AND B. RIVIÈRE, *On the solution of the coupled Navier–Stokes and Darcy equations*, Comput. Methods Appl. Mech. Engrg., 198 (2009), pp. 3806–3820, doi:10.1016/j.cma.2009.08.012.
- [32] O. CICEK, *Compositional and non-isothermal simulation of CO₂ sequestration in naturally fractured reservoirs/coalbeds: Development and verification of the model*, SPE-84341, PE Annual Technical Conference and Exhibition, Denver, CO, 2003, doi:10.2118/84341-MS.
- [33] C. D’ANGELO AND P. ZUNINO, *Robust numerical approximation of coupled Stokes’ and Darcy’s flows applied to vascular hemodynamics and biochemical transport*, ESAIM Math. Model. Numer. Anal., 45 (2011), pp. 447–476, doi:10.1051/m2an/2010062.
- [34] Y. DING, Y. WU, N. FARAH, C. WANG, AND B. BOURBIAUX, *Numerical simulation of low permeability unconventional gas reservoirs*, SPE-167711, SPE/EAGE European Unconventional Resources Conference and Exhibition, Vienna, Austria, 2014, doi:10.2118/167711-MS.
- [35] M. DISCACCIATI, *Domain Decomposition Methods for the Coupling of Surface and Groundwater Flows*, Ph.D. thesis, Ecole Polytechnique Fédérale de Lausanne, Lausanne, Switzerland, 2004, doi:10.5075/epfl-thesis-3117.
- [36] M. DISCACCIATI, E. MIGLIO, AND A. QUARTERONI, *Mathematical and numerical models for coupling surface and groundwater flows*, Appl. Numer. Math., 43 (2002), pp. 57–74, doi:10.1016/S0168-9274(02)00125-3.

- [37] M. DISCACCIATI, A. QUARTERONI, AND A. VALLI, *Robin–Robin domain decomposition methods for the Stokes–Darcy coupling*, SIAM J. Numer. Anal., 45 (2007), pp. 1246–1268, doi:10.1137/06065091X.
- [38] J. DOUGLAS, JR., AND T. DUPONT, *Galerkin methods for parabolic equations*, SIAM J. Numer. Anal., 7 (1970), pp. 575–626, doi:10.1137/0707048.
- [39] V. J. ERVIN, E. W. JENKINS, AND H. LEE, *Approximation of the Stokes–Darcy system by optimization*, J. Sci. Comput., 59 (2014), pp. 775–794, doi:10.1007/s10915-013-9779-8.
- [40] V. J. ERVIN, E. W. JENKINS, AND S. SUN, *Coupled generalized nonlinear Stokes flow with flow through a porous medium*, SIAM J. Numer. Anal., 47 (2009), pp. 929–952, doi:10.1137/070708354.
- [41] W. FENG, X.-M. HE, Z. WANG, AND X. ZHANG, *Non-iterative domain decomposition methods for a non-stationary Stokes–Darcy model with Beavers–Joseph interface condition*, Appl. Math. Comput., 219 (2012), pp. 453–463, doi:10.1016/j.amc.2012.05.012.
- [42] W. FRAUNHOFER AND G. WINTER, *The use of asymmetrical flow field-flow fractionation in pharmaceuticals and biopharmaceutics*, Eur. J. Pharm. Biopharm., 58 (2004), pp. 369–383, doi:10.1016/j.ejpb.2004.03.034.
- [43] J. GALVIS AND M. SARKIS, *FETI and BDD preconditioners for Stokes–Mortar–Darcy systems*, Commun. Appl. Math. Comput. Sci., 5 (2010), pp. 1–30, doi:10.2140/camcos.2010.5.1.
- [44] L. GÄRDING, *An inequality for hyperbolic polynomials*, J. Math. Mech., 8 (1959), pp. 957–965, doi:10.1512/iumj.1959.8.58061.
- [45] G. N. GATICA, R. OYARZÚA, AND F. J. SAYAS, *A residual-based a posteriori error estimator for a fully-mixed formulation of the Stokes–Darcy coupled problem*, Comput. Methods Appl. Mech. Engrg., 200 (2011), pp. 1877–1891, doi:10.1016/j.cma.2011.02.009.
- [46] H. H. GERKE AND M. T. VAN GENUCHTEN, *Evaluation of a first-order water transfer term for variably saturated dual-porosity flow models*, Water Resour. Res., 29 (1993), pp. 1225–1238, doi:10.1029/92WR02467.
- [47] H. H. GERKE AND M. T. VAN GENUCHTEN, *Macroscopic representation of structural geometry for simulating water and solute movement in dual-porosity media*, Adv. Water Resour., 19 (1996), pp. 343–357, doi:10.1016/0309-1708(96)00012-7.
- [48] J. R. GILMAN AND H. KAZEMI, *Improved calculations for viscous and gravity displacement in matrix blocks in dual-porosity simulators (includes associated papers 17851, 17921, 18017, 18018, 18939, 19038, 19361, and 20174)*, J. Petro. Technol., 40 (1988), pp. 60–70, doi:10.2118/16010-PA.
- [49] V. GIRAULT AND B. RIVIÈRE, *DG approximation of coupled Navier–Stokes and Darcy equations by Beaver–Joseph–Saffman interface condition*, SIAM J. Numer. Anal., 47 (2009), pp. 2052–2089, doi:10.1137/070686081.
- [50] V. GIRAULT, D. VASSILEV, AND I. YOTOV, *Mortar multiscale finite element methods for Stokes–Darcy flows*, Numer. Math., 127 (2014), pp. 93–165, doi:10.1007/s00211-013-0583-z.
- [51] C. GUO, M. WEI, H. CHEN, X. HE, AND B. BAI, *Improved numerical simulation for shale gas reservoirs*, OTC-24913, Offshore Technology Conference Asia, Kuala Lumpur, Malaysia, 2014, doi:10.4043/24913-MS.
- [52] N. HANSPAL, A. WAGHODE, V. NASSEHI, AND R. WAKEMAN, *Numerical analysis of coupled Stokes/Darcy flow in industrial filtrations*, Transp. Porous Media, 64 (2006), pp. 73–101, doi:10.1007/s11242-005-1457-3.
- [53] Y. HAO, P. FU, AND C. R. CARRIGAN, *Application of a dual-continuum model for simulation of fluid flow and heat transfer in fractured geothermal reservoirs*, in Proceedings of the Thirty-Eighth Workshop on Geothermal Reservoir Engineering, Stanford University, Stanford, CA, 2013.
- [54] N. W. HAWS, P. S. C. RAO, J. SIMUNEK, AND I. C. POYER, *Single-porosity and dual-porosity modeling of water flow and solute transport in subsurface-drained fields using effective field-scale parameters*, J. Hydrol., 313 (2005), pp. 257–273, doi:10.1016/j.jhydrol.2005.03.035.
- [55] X. HE, J. LI, Y. LIN, AND J. MING, *A domain decomposition method for the steady-state Navier–Stokes–Darcy model with Beavers–Joseph interface condition*, SIAM J. Sci. Comput., 37 (2015), pp. S264–S290, doi:10.1137/140965776.
- [56] R. HOPPE, P. PORTA, AND Y. VASSILEVSKI, *Computational issues related to iterative coupling of subsurface and channel flows*, Calcolo, 44 (2007), pp. 1–20, doi:10.1007/s10092-007-0126-z.
- [57] L. S. HOU, *Error estimates for semidiscrete finite element approximations of the Stokes equations under minimal regularity assumptions*, J. Sci. Comput., 16 (2001), pp. 287–317, doi:10.1023/A:1012869611793.
- [58] W. HUANG, G. D. DONATO, AND M. J. BLUNT, *Comparison of streamline-based and grid-based dual porosity simulation*, J. Petro. Sci. Eng., 43 (2004), pp. 129–137, doi:10.1016/j.petrol.2004.01.002.

- [59] G. KANSCHAT AND B. RIVIÈRE, *A strongly conservative finite element method for the coupling of Stokes and Darcy flow*, J. Comput. Phys., 229 (2010), pp. 5933–5943, doi:10.1016/j.jcp.2010.04.021.
- [60] H. KAZEMI, L. S. MERRILL, JR., K. L. PORTERFIELD, AND P. R. ZEMAN, *Numerical simulation of water-oil flow in naturally fractured reservoirs*, Soc. Petro. Eng., 16 (1976), pp. 317–326, doi:10.2118/5719-PA.
- [61] J. KIM, E. L. SONNENTHAL, AND J. RUTQVIST, *Formulation and sequential numerical algorithms of coupled fluid/heat flow and geomechanics for multiple porosity materials*, Internat. J. Numer. Methods Engrg., 92 (2012), pp. 425–456, doi:10.1002/nme.4340.
- [62] W. LAYTON, H. TRAN, AND C. TRENCH, *Analysis of long time stability and errors of two partitioned methods for uncoupling evolutionary groundwater–surface water flows*, SIAM J. Numer. Anal., 51 (2013), pp. 248–272, doi:10.1137/110834494.
- [63] W. J. LAYTON, F. SCHIEWECK, AND I. YOTOV, *Coupling fluid flow with porous media flow*, SIAM J. Numer. Anal., 40 (2003), pp. 2195–2218, doi:10.1137/S0036142901392766.
- [64] K. T. LIM AND K. AZIZ, *Matrix-fracture transfer shape factors for dual-porosity simulators*, J. Petro. Sci. Eng., 13 (1995), pp. 169–178, doi:10.1016/0920-4105(95)00010-F.
- [65] A. MÁRQUEZ, S. MEDDAHI, AND F. J. SAYAS, *A decoupled preconditioning technique for a mixed Stokes-Darcy model*, J. Sci. Comput., 57 (2013), pp. 174–192, doi:10.1007/s10915-013-9700-5.
- [66] C. A. MORA AND R. A. WATTENBARGER, *Analysis and verification of dual porosity and CBM shape factors*, J. Can. Petro. Technol., 48 (2009), pp. 17–21, doi:10.2118/09-02-17.
- [67] M. MU AND J. XU, *A two-grid method of a mixed Stokes–Darcy model for coupling fluid flow with porous media flow*, SIAM J. Numer. Anal., 45 (2007), pp. 1801–1813, doi:10.1137/050637820.
- [68] M. MU AND X. ZHU, *Decoupled schemes for a non-stationary mixed Stokes–Darcy model*, Math. Comp., 79 (2010), pp. 707–731, doi:10.1090/S0025-5718-09-02302-3.
- [69] S. MÜNZENMAIER AND G. STARKE, *First-order system least squares for coupled Stokes–Darcy flow*, SIAM J. Numer. Anal., 49 (2011), pp. 387–404, doi:10.1137/100805108.
- [70] V. NASSEHI, *Modelling of combined Navier-Stokes and Darcy flows in crossflow membrane filtration*, Chem. Eng. Sci., 53 (1998), pp. 1253–1265, doi:10.1016/S0009-2509(97)00443-0.
- [71] E. RANJBAR AND H. HASSANZADEH, *Matrix–fracture transfer shape factor for modeling flow of a compressible fluid in dual-porosity media*, Adv. Water Resour., 34 (2011), pp. 627–639, doi:10.1016/j.advwatres.2011.02.012.
- [72] C. RAY, T. R. ELLSWORTH, A. J. VALOCCHI, AND C. W. BOAST, *An improved dual porosity model for chemical transport in macroporous soils*, J. Hydrol., 193 (1997), pp. 270–292, doi:10.1016/S0022-1694(96)03141-1.
- [73] P. RESCHIGLIAN AND M. H. MOON, *Flow field-flow fractionation: A pre-analytical method for proteomics*, J. Proteomics, 71 (2008), pp. 265–276, doi:10.1016/j.jprot.2008.06.002.
- [74] B. RIVIÈRE AND I. YOTOV, *Locally conservative coupling of Stokes and Darcy flows*, SIAM J. Numer. Anal., 42 (2005), pp. 1959–1977, doi:10.1137/S0036142903427640.
- [75] I. RYBAK AND J. MAGIERA, *A multiple-time-step technique for coupled free flow and porous medium systems*, J. Comput. Phys., 272 (2014), pp. 327–342, doi:10.1016/j.jcp.2014.04.036.
- [76] S. SARKAR, M. N. TOKSOZ, AND D. R. BURNS, *Fluid Flow Simulation in Fractured Reservoirs*, Technical report, Earth Resources Laboratory, Massachusetts Institute of Technology, Cambridge, MA, 2002.
- [77] R. A. SEALE AND J. ATHANS, *An effective openhole horizontal completion system for multistage fracturing and stimulation*, Society of Petroleum Engineers, SPE Tight Gas Completions Conference, 2008, doi:10.2118/114880-MS.
- [78] R. A. SEALE, J. DONALDSON, AND J. ATHANS, *Multistage fracturing system: Improving operational efficiency and production*, Society of Petroleum Engineers, SPE Eastern Regional Meeting, 2006, doi:10.2118/104557-MS.
- [79] A. R. SHAIKA, S. S. RAHMANA, N. H. TRANA, AND T. TRAN, *Numerical simulation of Fluid-Rock coupling heat transfer in naturally fractured geothermal system*, Appl. Therm. Eng., 31 (2011), pp. 1600–1606, doi:10.1016/j.applthermaleng.2011.01.038.
- [80] J. R. SILVEIRA, A. G. HUGHSON, AND B. CAUGHEY, *Fractionation of prion protein aggregates by asymmetrical flow field-flow fractionation*, Methods Enzymol., 412 (2006), pp. 26–33, doi:10.1016/S0076-6879(06)12002-9.
- [81] J. J. SMOLEN, *Cased Hole and Production Log Evaluation*, PennWell Books, Tulsa, OK, 1996.
- [82] T. D. STRELTSAVA-ADAMS, *Fluid flow in naturally fractured reservoirs*, in Proceedings of the 2nd Invitational Well-Testing Symposium, Lawrence Berkeley Laboratory, University of California, Berkeley, CA, 1978, pp. 71–77.
- [83] V. THOMÉE, *Galerkin Finite Element Methods for Parabolic Problems*, 2nd ed., Springer Ser.

- Comput. Math. 25, Springer-Verlag, Berlin, 2006, doi:10.1007/3-540-33122-0.
- [84] S. TLUPOVA AND R. CORTEZ, *Boundary integral solutions of coupled Stokes and Darcy flows*, J. Comput. Phys., 228 (2009), pp. 158–179, doi:10.1016/j.jcp.2008.09.011.
- [85] Y. UEDA, S. MURATA, Y. WATANABE, AND K. FUNATSU, *Investigation of the shape factor used in the dual-porosity reservoir simulator*, SPE-19469, Society of Petroleum Engineers, SPE Asia-Pacific Conference, Sydney, Australia, 1989, doi:10.2118/SPE-19469-MS.
- [86] D. VASSILEV AND I. YOTOV, *Coupling Stokes–Darcy flow with transport*, SIAM J. Sci. Comput., 31 (2009), pp. 3661–3684, doi:10.1137/080732146.
- [87] W. WANG AND C. XU, *Spectral methods based on new formulations for coupled Stokes and Darcy equations*, J. Comput. Phys., 257, part A (2014), pp. 126–142, doi:10.1016/j.jcp.2013.09.036.
- [88] J. E. WARREN AND P. J. ROOT, *The behavior of naturally fractured reservoirs*, Soc. Petrol. Eng. J., 3 (1963), pp. 245–255, doi:10.2118/426-PA.
- [89] M. F. WHEELER, *A priori L_2 error estimates for Galerkin approximations to parabolic partial differential equations*, SIAM J. Numer. Anal., 10 (1973), pp. 723–759, doi:10.1137/0710062.
- [90] J. YAO, Z. HUANG, Y. LI, C. WANG, AND X. LV, *Discrete fracture-vug network model for modeling fluid flow in fractured vuggy porous media*, Society of Petroleum Engineers, International Oil and Gas Conference and Exhibition, Beijing, China, 2010, doi:10.2118/130287-MS.
- [91] R. W. ZIMMERMAN, G. CHEN, T. HADGU, AND G. S. BODVARSSON, *A numerical dual-porosity model with semianalytical treatment of fracture/matrix flow*, Water Resour. Res., 29 (1993), pp. 2127–2137, doi:10.1029/93WR00749.